

## ABSTRACT

### ANALYSIS AND DEVELOPMENT OF A LOWER EXTREMITY OSTEOLOGICAL MONITORING TOOL BASED ON VIBRATION DATA

by Jacob Evan Veta

Vibration based monitoring techniques are widely used to detect damage, monitor the growth of inherent defects, system identification, and material parameter estimation for various engineering applications. These techniques present a non-invasive and relatively inexpensive tool for various biomedical applications, for example, in characterizing the mechanical properties of the bone and muscles of humans as well as animals. In recent years, it has been shown that fundamental natural frequencies and corresponding damping ratios can be correlated to the bone health quality indicators as associated with osteoporosis, osteoarthritis etc. In this research, through the investigation of clinical data, an analysis procedure is developed to investigate the correlation between the damping properties associated with both lower and higher modes of vibration and bone health quality. Subsequently, a data-driven system identification tool for reconstructing the parameters (mass, stiffness, damping distributions) in a low-dimensional human model is developed which utilizes selected measurements from the clinical study. It is anticipated that the analysis process and parameter identification techniques presented here can be developed and tuned for any individual human model and can be used as osteological monitoring tool for predicting early diagnostics pre-cursors of the bone or muscle related conditions or diseases.

ANALYSIS AND DEVELOPMENT OF A LOWER EXTREMITY OSTEOLOGICAL  
MONITORING TOOL BASED ON VIBRATION DATA

A Thesis

Submitted to the

Faculty of Miami University

in partial fulfillment of

the requirements for the degree of

Master of Science

by

Jacob Evan Veta

Miami University

Oxford, Ohio

2020

Advisor: Kumar Singh

Reader: James Chagdes

Reader: Mark Walsh

©2020 Jacob Evan Veta

This Thesis titled

ANALYSIS AND DEVELOPMENT OF A LOWER EXTREMITY OSTEOLOGICAL  
MONITORING TOOL BASED ON VIBRATION DATA

by

Jacob Evan Veta

has been approved for publication by

The College of Engineering and Computing

and

Department of Mechanical and Manufacturing Engineering

---

Kumar Singh

---

James Chagdes

---

Mark Walsh

# Table of Contents

<b>1. INTRODUCTION.....</b>	<b>1</b>
1.1 Aging and Bones .....	1
1.2 Fundamentals of Bone Densitometry .....	1
1.3 Vibration Based Monitoring.....	4
1.4 Human Vibration Testing .....	5
1.5 Human Vibration Models .....	7
1.6 Fundamentals of Vibration Analysis .....	10
1.7 Motivation of Research .....	11
1.8 The Problem Statement .....	12
<b>2. MODAL PARAMETER EXTRACTION AND STATISTICAL ANALYSIS OF CLINICAL DATA .....</b>	<b>15</b>
2.1 Subject Data .....	15
2.2 Frequency and Damping.....	17
2.3 Preliminary Statistical Analysis.....	22
2.4 Density Based Spatial Clustering of Applications with Noise .....	24
2.5 Clustering Parameters.....	25
2.6 Implementation.....	26
2.7 Bin-Based Mode Criteria.....	32
2.8 Groupwise Analysis of Variance.....	34
2.9 Limitations and Improvements.....	38
<b>3. DEVELOPMENT OF A SYSTEM IDENTIFICATION MODEL .....</b>	<b>40</b>
3.1 Background .....	40
3.2 Basic Algorithms .....	40
3.3 Simple Batch Gradient Descent Method .....	41
3.4 Gauss Newton Method .....	44
3.5 Levenberg-Marquardt.....	44
3.6 Influences on Identification Quality .....	45
3.7 Human Model Structure .....	54
3.8 Initial System Estimation Algorithm .....	57
3.9 Application of Analytical Estimation .....	59
3.10 Parameter Estimation using System Identification Toolbox.....	66
3.11 Effects of Body Mass Index on Identified Parameters .....	71
<b>4. CONCLUSION .....</b>	<b>74</b>
4.1 Summary of results.....	74
4.2 Discussion .....	76
<b>5. REFERENCES.....</b>	<b>80</b>

## List of Tables

Table 1: Validation of average time-domain signal.....	18
Table 2: Frequency bin ranges.....	21
Table 3: First Mode: ~30hz.....	29
Table 4: Second Mode: ~250hz.....	30
Table 5: Third Mode: ~450hz.....	30
Table 6: Global bin boundaries for Mode 1, by sensor.....	32
Table 7: Global bin boundaries for Mode 2, by sensor.....	32
Table 8: Global bin boundaries for Mode 3, by sensor.....	33
Table 9: Means of each sensor boundaries, by mode .....	33
Table 10: First Mode: ~30hz.....	33
Table 11: Second Mode: ~250hz.....	34
Table 12: Third Mode: ~450hz.....	34
Table 13: LBK cluster ANOVA.....	35
Table 14: LAK cluster ANOVA.....	35
Table 15: RBK cluster ANOVA.....	35
Table 16: RAK cluster ANOVA.....	36
Table 17: LBK bin ANOVA.....	36
Table 18: LAK bin ANOVA.....	36
Table 19: RBK bin ANOVA.....	36
Table 20: RAK bin ANOVA .....	37
Table 21: Kim model parameters [34,35].....	46
Table 22: Parameters for re-identified system.....	50
Table 23: Parameters for estimation with compounding error estimation.....	53
Table 24: Human body mass distribution.....	55
Table 25: Estimated mass distribution for subject 1.....	59
Table 26: First four frequency damping pair for subject 1.....	62
Table 27: Initial estimates of stiffness and damping parameters for subject 1.....	62
Table 28: Estimated initial conditions from curve fit.....	65
Table 29: System parameters with estimable stiffness.....	66
Table 30: System parameters with estimable stiffness and damping.....	68
Table 31: System parameters with estimable mass, stiffness, and damping.....	69
Table 32: Estimated values for model elements.....	71
Table 33: Identified modes for three subjects with varying mass.....	72
Table 34: Comparative analysis of subjects with varying mass.....	72

## List of Figures

Figure 1: Diagram of a typical human long bone [7].....	2
Figure 2: Typical clinical bone-densitometer [10].....	3
Figure 3: DEXA bone densitometer patent sketch [13].....	3
Figure 4: Angular motion model of a runner, from Kim et. al [23].....	5
Figure 5: Seated human body model [31].....	7
Figure 6: Standing human body subjected to base excitation [32] .....	8
Figure 7: Klute-Berge GRF Model [33,34] .....	9
Figure 8: Kim et. al model [34,35] .....	10
Figure 9: Schematic of accelerometer placement [38] .....	15
Figure 10: Sensor orientation in relation to skeleton.....	16
Figure 11: Characteristic time-domain signals from BSA experiment.....	17
Figure 12: Example of a typical BSA FRF (10-250 Hz) .....	19
Figure 13: Modal stabilization diagram.....	20
Figure 14: Phase angle plot for estimation of modes.....	20
Figure 15: Frequency bin sets, graphical .....	21
Figure 16: Curve fit for mode estimation of upper set 2 frequency range.....	22
Figure 17: Frequency histograms for all subjects .....	23
Figure 18: Filtered frequency histograms for all subjects .....	23
Figure 19: Scatter plots for all tests .....	24
Figure 20: Example of a plot of sorted Euclidean distances.....	26
Figure 21: DBSCAN results with $epmod = 1$ .....	27
Figure 22: DBSCAN results with $epmod = 0.4$ .....	28
Figure 23: DBSCAN results for the below-knee sensor for quartile 1 .....	29
Figure 24: ANOVA of Modes 1 and 2 for Group 1 LBK.....	31
Figure 25: ANOVA of Modes 1 and 3 for Group 1 LBK.....	31
Figure 26: Groupwise ANOVA example, Mode 2, LBK, 1 vs 4.....	37
Figure 27: Demonstration of graphical BSA toolbox .....	39
Figure 28: Linear gradient descent example.....	42
Figure 29: Changes in the cost function with each iteration.....	43
Figure 30: Kim et. al model [34,35] .....	45
Figure 31: Simulated Kim model with 100 N / 0.1 s impulse .....	48
Figure 32: Displacement channels for re-identified system .....	49
Figure 33: Identified displacement channels with random noise.....	50
Figure 34: Effects of proportional damping assumption on estimation.....	51
Figure 35: Effects of missing data channel on estimation .....	52
Figure 36: Effects of several compounding error sources .....	53
Figure 37(a-c): Human body mass segments, 3dof vibrational models.....	54
Figure 38: Time domain data for one mass and a single test.....	60
Figure 39: Example of modal stabilization diagram used to estimate curve order.....	61
Figure 40: Example of fitted curve for mode pair identification .....	61
Figure 41: Comparison of simulated and experimental responses .....	63

Figure 42: Comparison of responses with modified mass distribution.....	63
Figure 43: Fitted curves for determination of initial conditions .....	64
Figure 44: Comparison of responses with initial velocity condition .....	65
Figure 45: Identified system with estimable stiffness.....	67
Figure 46: Comparison of experimental data, initial system, and identified system for verification .....	67
Figure 47: Identified system with estimable stiffness and damping.....	68
Figure 48: Identified acceleration response with free mass, stiffness, and damping.....	70
Figure 49: Identified acceleration response with bounded mass, free stiffness and damping.....	70
Figure 50: Estimated stiffness plotted against subject BMI .....	73
Figure 51: Vertical displacement due to transverse flexural motion .....	77
Figure 52: Placement of additional accelerometers .....	78

## **Dedication**

To my grandmother Victoria, and the memory of my grandfather Albert.

I will be forever grateful for your love and support.

## **Acknowledgements**

This study was partially supported by a NIEHS grant 1R01ES024074-01 (Bhattacharya). The BSA technology used in this study is a patented device under the name of last author Bhattacharya (Patent : 2014-Serial No. 12/402,586).

# 1. Introduction

## 1.1 *Aging and Bones*

Bone is a living tissue, and human aging is typically accompanied by gradual bone loss. Low bone density in osteoporosis patients has been found to have appreciable impact on fracture risk, which poses significant dangers to elderly patients. Bone loss greater than 2.5 standard deviations from the healthy mean is classified as osteoporosis, affecting about 10 million Americans. Osteoporosis and bone loss together affect about 54 million older Americans, and post-menopausal women are at especially high risk [1–3]. While contemporary diagnostic tools do well at categorizing bone qualities, they do not provide insight into dynamic or gradual degradation of bone/muscle health that impact fracture risk. Increasing life expectancies are predicted to cause an increase in hip fracture incidence by around 275% by 2050 [4], signaling increased demand for diagnostic tools. Regular screening is recommended for all post-menopausal women, and patients with borderline osteoporosis require yearly screening [5]. The increasing need for screening tools and limitations of current methods necessitate the development of novel methods.

## 1.2 *Fundamentals of Bone Densitometry*

Skeletal bone is a composite with highly variable geometry and composition. Primarily, this composite is composed of a matrix consisting of collagen and mineral deposits that grow on this matrix. Two types of skeletal bone form most of the structure, cortical and trabecular bone, often referred to as hard and spongy bone, respectively. Cortical bone forms the hard, off-white outer layer that the layman would typically call bone. Trabecular bone is primarily present in the largest quantities at the ends of long bones, but a layer of trabecular bone is also present towards the ends of the medullary cavity. While both materials contribute to the global stiffness and damping properties of the composite structure, cortical bone provides the majority of the elastic

stiffness, while the softer trabecular bone provides much of the structural damping [6]. A diagram of these types of bone is shown below in Figure 1 below.

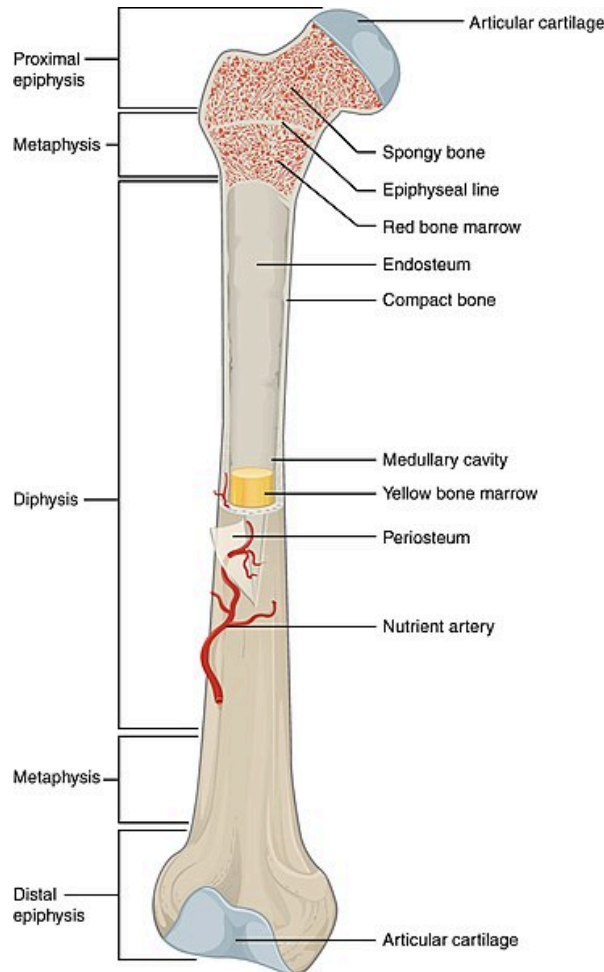


**Figure 1:** Diagram of a typical human long bone [7]

Throughout the first half of the 20<sup>th</sup> century, incidence of fracture and anomalies in trabecular bone distribution were taken as primary indicators of osteoporosis. Bone mineral density (BMD) refers to the density measurement of calcium deposits on the collagen matrix. Modern methods of detecting osteoporosis using radiographic measurement tools now allows BMD to be directly determined before fractures occur [8]. The contemporary method of BMD measurement utilizes Dual Energy X-ray Absorptiometry (DEXA). With this method, low-dose x-rays of two different energy levels are used to allow for the effective imaging of composites

consisting of component materials with widely differing densities. This method is now the most widely employed method, and today serves as the primary tool used to diagnose and track the progress of osteoporosis as well predict fracture risk at specific sites [9]. A photograph of a typical GE ARIA DEXA based bone densitometer is shown below in Figure 2 below.



**Figure 2:** Typical clinical bone-densitometer [10]

A more detailed diagram of the DEXA system from a US patent is shown in Figure 3 below. Fan-beam geometry X-rays are generated by a moving emitter beneath the patient. X-rays that are not blocked by the patient's body are collected in the detector array above the patient, moving in tandem with the emitter below. The use of X-rays of varying energies allow DEXA to simultaneously measure image hard and soft tissues. Patients are typically exposed to no more than 0.0105 mSv (millisieverts), which is far below 50 mSv maximum yearly dosage recommended by the US federal government [11,12].

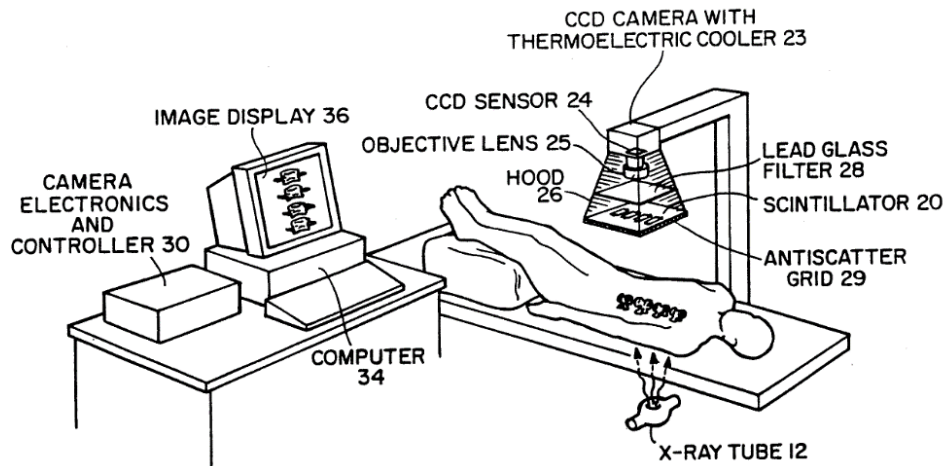


**Figure 3:** DEXA bone densitometer patent sketch [13]

DEXA based measurement of BMD requires sizeable and expensive equipment, necessitating the measurement be carried out in a clinical environment, which presents issues of convenience and cost for patients who need regular screening as well as requiring one or more clinicians to operate the machine. Additionally, the DEXA method is limited to static, geometric measurements and does not capture elastic modulus, structural damping, or any other dynamic qualities, which have been shown to impact bone strength and fracture resistance. There are reports that BMD alone is not an effective predictor of fracture risk, and older patients with healthy BMD measurements may still face a 10-fold increase in fracture risk [14]. These disadvantages presented by DEXA necessitate the development of new non-invasive, low cost, and high convenience methods for measuring the progression of life-long bone diseases.

### **1.3 *Vibration Based Monitoring***

By continually monitoring the dynamic data (time or frequency domain) for a system, changes in geometry or material properties may be predicted, detected, and located. Vibration-based monitoring (VBM) is typically nondestructive, relying on sensors such as accelerometers mounted to a structure to continuously monitor its health. These sensors may be relatively small, lightweight, and consume little power. This makes VBM attractive for applications where destructive testing is not practical, size and weight are a concern, and monitoring must be continuous. In applications such as civil engineering and aviation, where material properties and geometry are known, such methods have been widely adopted and used for decades [15–17].

Naturally these aspects make the use of VBM for the tracking of material changes in human subjects highly desirable. The simplicity of the equipment makes VBM easier and less expensive to implement outside of a clinical setting compared to DEXA. Such a system could be implemented in emerging smart wearable technology to allow patients and their clinicians the ability to track bone degradation in real time while reducing the need for costly and invasive laboratory checkups [18]. Initial experiments have investigated the use of this method for tracking the progress of osteoporosis, a widespread condition that primarily effects the elderly and leads to increased risk of skeletal fracture [6,19]. Existing smartphone accelerometers are approaching sampling rates near 200 Hz. and are rapidly improving, suggesting that existing technology may

be useful in this application in the coming years [20]. Additionally, new technologies such as the pressure-measuring insoles and accelerometer-containing garments can allow this technology to leave the lab and monitor patients in their day-to-day lives [21,22].

#### 1.4 *Human Vibration Testing*

Vibration testing of human subjects for clinical analysis is a well-studied subject with applications in osteopathic medicine, biomechanics, sports performance, footwear design, and workplace safety, among other fields. Difficulties in isolation of the system desired for analysis are compounded by several factors.

The foot-ground mechanism, which is defined as the combination of the fat pad at the base of the heel, the sole of the shoe, and the compliance of the striking surface can influence both the amplitude of the shock wave transmitted through the body and the amplitude of the ground reaction force. Kim et. al demonstrated that changes in foot-ground mechanism stiffness in a running subject, and therefore changes in the natural frequency of the system, do not have a significant effect on the ground reaction force, but do influence the loading rate and therefore the amplitude of the transmitted shockwave [23]. However, an increase in the damping factor results in a linear decrease in the ground reaction force and doubling the damping value of the foot-ground mechanism reduces the ground reaction force by about 10%. In addition, they propose a single degree-of-freedom model that considers the transverse motion of the human subject in combination with the linear motion of the foot-ground mechanism, shown in Figure 4.

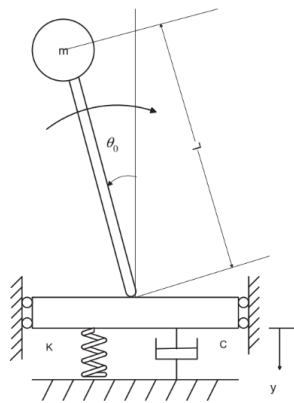


**Figure 4:** Angular motion model of a runner, from Kim et. al [23]

While the models presented in this thesis will approximate the human body as a passive system, this is not entirely accurate. Kim et. al also demonstrated that leg stiffness is modified to comply with changes in the running surface while maintaining the natural running mechanics of the subject. Further evidence suggests the body actively seeks to minimize soft tissue vibration by adjusting muscle activity in the lower extremities in order to optimize landing for the intrinsic dynamics of the human system [24–27]. Factors such as shoe material, surface compliance, and gait all effect how and which muscles are activated in muscle tuning.

The experiment that forms the basis of this thesis relies on accelerometers secured to the test subject as the skin using double-sided tape but seeks to identify the vibrational dynamics of the underlying bone. Ziegert and Lewis investigated the differences in mechanical properties of these two materials in a 1979 study [28]. An experiment was performed to simultaneously measure the acceleration of both the skin and the bone at the shank of a living subject subjected to an impulse excitation at the medial malleolus just above the ankle joint. Acceleration at the skin was measured with an accelerometer secured with an elastic strap, while acceleration at the bone was measured by inserting a needle in direct contact with the bone with an attached low-mass accelerometer. They found that the mechanical stiffness of the skin was on the order of  $10^6$ , while the stiffness of the bone was on the order of  $10^8$ . They conclude that the dominant natural frequency of bone is approximately 2000 Hz, and the response of the relatively heavy skin-mounted accelerometer is unrelated to the bone acceleration.

In addition to the Ziegert and Lewis study which sought to determine the dynamics of bone within a human subject, other studies have focused on the behavior of the unloaded dry bone – that is, the bone by itself, separated from a cadaver or animal test subject and without the presence of the surrounding soft tissues. Hight et. al’s analysis of a dry human tibia indicate the first dominant axial frequency of the bone to be between approximately 2000 Hz and 4000 Hz depending on the boundary constraint conditions, consistent with Ziegert and Lewis’ findings [29]. Impulse excitation experiments performed by Thomsen also conclude that dry bone vibrates at a relatively high frequency compared to the surrounding soft tissue, with results indicated an axial natural frequency at 3250 Hz [30]. In all of these experiments, flexural frequencies were found to be much lower, beginning at 200 Hz.

## 1.5 Human Vibration Models

Several models have been proposed to represent the axial, or vertical dynamics of the human body under loading. The motion of the models, given by  $z_i$  and  $x_i$ , as shown in Figure 4 and 5 respectively, depend on the structural parameters and the input force. The natural frequencies and damping ratios associated with vibration modes can be obtained by determining the eigenvalues of the governing equations of motion. Many past studies have focused on the human body in the sitting position, as these models are typically developed to represent an operator of some piece of equipment. Boileau et al. provide an example of a seated whole-body, shown in Figure 5 below [31].

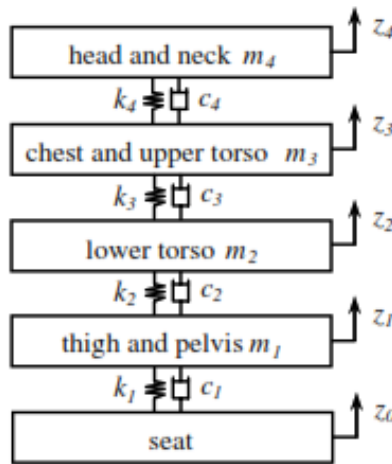


**Figure 5:** Seated human body model [31]

For standing humans, several more sophisticated models have been developed as well. The example shown in Figure 6, developed by Gupta et al., represents the human body in the standing position, with motion along vertical axis [32]. This model is subjected to a “base excitation”, where the excitation phenomenon is displacement of the platform on which the subject is standing. In this research these types of discrete models will be used for system identification purposes and the model parameters will be obtained based on available time and frequency domain clinical data.

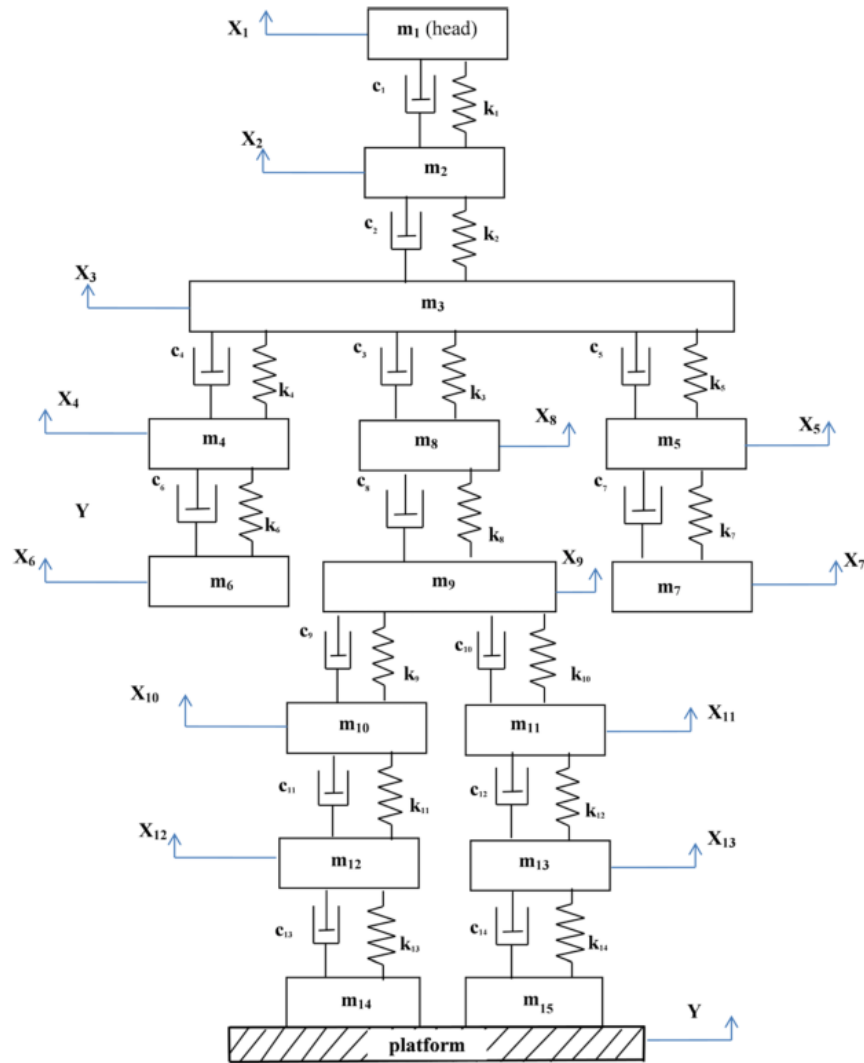


**Figure 6:** Standing human body subjected to base excitation [32]

These two models are generalized representations of the human body structure. For the specific application of studying base excitation of the standing posture, more specific models have been developed. The parameters of mass, stiffness, and damping can be assembled and related via differential equations to determine the response of the system to some excitation. Klute and Berge propose a five-body model that represents the ground-reaction-force as a spring-damper combination connecting the lower-most mass to the ground [33]. This model is shown in Figure 7 below.

$$\begin{aligned}
\mathbf{M}: & \begin{bmatrix} m_1 & 0 & 0 & 0 & 0 \\ 0 & m_2 & 0 & 0 & 0 \\ 0 & 0 & m_3 & 0 & 0 \\ 0 & 0 & 0 & m_4 & 0 \\ 0 & 0 & 0 & 0 & m_5 \end{bmatrix} & \mathbf{C}: & \begin{bmatrix} c_2 & -c_2 & 0 & 0 & 0 \\ -c_2 & c_2 + c_3 & -c_3 & 0 & 0 \\ 0 & -c_3 & c_3 + c_4 & -c_4 & 0 \\ 0 & 0 & -c_4 & c_4 + c_5 & -c_5 \\ 0 & 0 & 0 & -c_5 & c_5 \end{bmatrix} \\
\mathbf{K}: & \begin{bmatrix} k_2 & -k_2 & 0 & 0 & 0 \\ -k_2 & k_2 + k_3 & -k_3 & 0 & 0 \\ 0 & -k_3 & k_3 + k_4 & -k_4 & 0 \\ 0 & 0 & -k_4 & k_4 + k_5 & -k_5 \\ 0 & 0 & 0 & -k_5 & k_5 \end{bmatrix} & \mathbf{F}: & \begin{bmatrix} m_1 g - F_G \\ m_2 g \\ m_3 g \\ m_4 g \end{bmatrix}
\end{aligned} \tag{1.1}$$

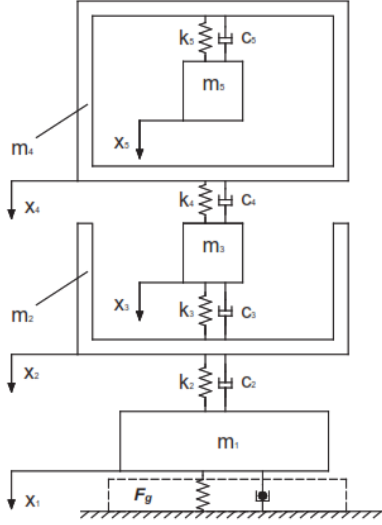


**Figure 7:** Klute-Berge GRF Model [33,34]

The Klute-Berge model does not couple the lowermost mass to the fixed platform with a spring and damper. Those elements in the graphical model serve as an approximation of the ground-reaction-force  $F_G$ , and are parameterless. Let us consider the model proposed by Kim et al. [35], shown in Figure 8 below.

$$\mathbf{M}: \begin{bmatrix} m_1 & 0 & 0 \\ 0 & m_2 & 0 \\ 0 & 0 & m_3 \end{bmatrix} \quad \mathbf{C}: \begin{bmatrix} c_1 + c_2 & -c_2 & 0 \\ -c_2 & c_2 + c_3 & -c_3 \\ 0 & -c_3 & c_3 \end{bmatrix} \quad \mathbf{K}: \begin{bmatrix} k_1 + k_2 & -k_2 & 0 \\ -k_2 & k_2 + k_3 & -k_3 \\ 0 & -k_3 & k_3 \end{bmatrix} \quad \mathbf{F}: \begin{bmatrix} m_1 g \\ m_2 g \\ m_3 g \end{bmatrix} \tag{1.2}$$

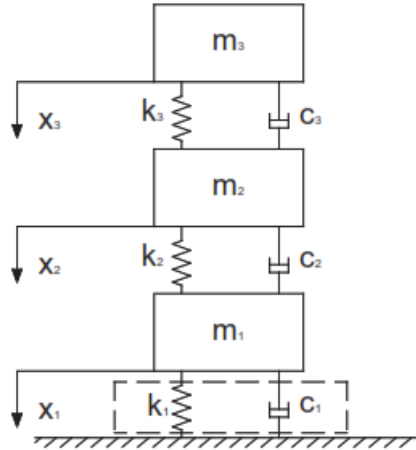


**Figure 8:** Kim et. al model [34,35]

This model includes the boundary parameters  $k_1$  and  $c_1$  as estimable model parameters, and constraining the model to the stationary platform with these elements results in a model that is generally stable, which makes linear estimation of model parameters possible. Note that the force matrix includes the gravitational force but no excitation force.

## 1.6 *Fundamentals of Vibration Analysis*

Continuous physical systems may be modeled as lumped-sum parameter models with mass, spring, and damper elements. When excited, systems composed of these elements tend to oscillate. Spring elements provide mechanical stiffness, while damping elements serve to oppose the oscillatory motion. The damping ratio  $\zeta$  describes the rate at which oscillations tend to die out in relation to the frequency. Oscillations can be described by their frequency and amplitude. The natural frequencies are those at which systems tend to oscillate with continuously increasing amplitude with time. These frequencies, along with their associated damping ratios are related to the modes of the system which indicates the direction of motion of each element with respect to each other. Continuous systems have a theoretically infinite number of these modes, but their determination is limited by measurement devices. Discrete models approximate realistic system into  $n \times n$  discrete systems, with  $n$  number of vibration modes.

Motion of a linear multiple-degree-of-freedom system can be represented by the following time domain differential equation of motion [36]:

$$\mathbf{M}\ddot{\mathbf{x}} + \mathbf{C}\dot{\mathbf{x}} + \mathbf{K}\mathbf{x} = \mathbf{f}(t) \quad (1.3)$$

where  $\mathbf{M}$ ,  $\mathbf{C}$  and  $\mathbf{K}$  are mass, damping and stiffness matrices respectively. The input excitation is represented by the force vector  $\mathbf{f}$ . For multiple degree-of-freedom systems, system matrices ( $\mathbf{M}, \mathbf{C}, \mathbf{K}$ ) take the form of  $n \times n$  matrices where  $n$  is the number of degrees of freedom. This equation can be transformed into the Laplace domain to determine its transfer function:

$$(s^2\mathbf{M} + s\mathbf{C} + \mathbf{K})\mathbf{X}(s) = \mathbf{F}(s) \quad (1.4)$$

The transfer function  $\mathbf{H}(s)$  represents the output response (sensor measurement) for a given excitation input and it can be written as follows:

$$\mathbf{H}(s) = \frac{\mathbf{X}(s)}{\mathbf{F}(s)} = (s^2\mathbf{M} + s\mathbf{C} + \mathbf{K})^{-1} \quad (1.5)$$

The roots of denominator polynomial of this function can be used in computing the natural frequencies and damping ratios of the system from the following equation:

$$s_i = -\zeta\omega_n \pm \omega_n\sqrt{1 - \zeta^2} \quad (1.6)$$

For the methods described in later sections of this work,  $\mathbf{H}(s)$  is known for the prescribed input and the system parameters defining  $\mathbf{M}$ ,  $\mathbf{C}$ , and  $\mathbf{K}$  are to be estimated, while accommodating physical constraints on these parameters related to the human body parts (bone/muscle stiffness etc.) of lower extremities.

## 1.7 Motivation of Research

The damping factor of a bone segment may provide insight into bone quality, as a decrease in damping factor corresponds to a decrease in density [37]. Bhattacharya et al. have demonstrated an approach to measure bone quality in humans through VBM. This study describes a method of distinguishing between patients with and without past fractural damage by measuring bone shock absorption (BSA) via the damping property  $\zeta$ , when traditional methods such as absorptiometry based bone mineral density (BMD) and static biomechanical analysis failed to. The authors conclude that the “dynamic bone quality” property damping factor,  $\zeta$  is an aggregate response of

bone's structural integrity under 'realistic' in-vivo loading. The bone's response under realistic dynamic loading provides a better picture of its structural integrity than that obtained under unloaded condition as structural failure of human bone and/or any mechanical system rarely occurs under static conditions" [38]. They go on to state that BSA techniques may be used to quantify bone health in patients with other osteopathic disorders such as osteoporosis in a manner potentially less invasive and costly than those employed by contemporary DEXA techniques. For some population such as children, DEXA alone is an insufficient means of predicting future fracture risk, necessitating novel methods of quantifying bone health and predict its behavior under load [39].

Other studies have proposed a quality factor based on the material damping factor and vibration modal damping factor, while this method takes the vibrational factor obtained as a direct measurement of bone quality. The measurement of live subjects is more easily performed via an impulse-response measurement rather than the frequency sweep method proposed by Panteliou et al [40]. These attributes make Bhattacharya et al.'s proposed method relatively easily to implement in comparison to other methods.

## **1.8    *The Problem Statement***

The method employed by Bhattacharya et. al describes the damping ratio at the first natural frequency, which appears to be around 15hz – 100hz [38]. Experimentally, the human tibia has been demonstrated to have a first natural frequency significantly higher than this range [28–30]. While the muscles, connective, and other tissues can be expected to have a much lower stiffness than the encompassed bone, even in combination these tissues cannot account for the significant decrease in natural frequency. This first mode may correspond to dynamics other than those of the skeletal, such as postural sway, displacement of the joints, or oscillation of the skin-mounted sensors rather than the underlying structures. The vibration characteristics changes significantly (on a scale) based on the measurement of individual body parts (tibia, femur etc.) or the overall human vibration. This is reflected in the clinical data provided by UC researchers for their BSA study towards investigating the effect of lead quantity on the bone health. Therefore, the overall goal of the proposed research is to investigate the variation in vibration characteristics (natural

frequencies and damping ratio) of the patient data obtained for the clinical study. The hypothesis is that the higher frequencies and their corresponding damping ratios will provide more accurate and consistent correlation compare to those obtained for lower frequencies.

In particular, clinical data obtained by UC researchers for an experimental setup will be analyzed for vibration characteristics by extracting frequency-response functions (FRFs) from the test data. Frequency-damping pairs identified from these FRFs will be used as a basis for statistical determination of the model order. These frequency-damping pairs can be concatenated, and high-density spatial regions will be identified to find the dominant natural vibrational frequencies and their corresponding damping values. As the BSA technique takes damping values at lower frequencies as the measure of bone health, finding these dominant modes (lower and higher modes) serves the dual-purpose of providing insight into expected lower extremity dynamics and identifying higher frequency regions that could serve to negate the effects of soft tissue vibration. Through systematic clustering and statistical analysis, the damping values of higher modes will be compared between groups with known differences in bone composition. Once the modal parameters (frequencies and damping ratios) are correlated with the bone composition they will become the basis for system identification for reconstructing human models and tracking the quality of bone for a specific patient

For these data to be useful in the diagnosis of osteopathic disorders, a model that approximates the human lower extremities must be developed through system identification techniques and will be validated using the available clinical data. A human model representing the dominant modes will be assumed, and system identification techniques applied to either individual or combined FRFs to estimate the model parameters (stiffness and damping associated with the bone/muscle) of the model. These parameters provide insight into the implications of the BSA metric and how it pertains to structural changes in the bone. Additionally, successful identification of higher order models may be used to indicate the spatial location of abnormalities or degeneration. In this research, by defining a grey box model of the structure system identification to determine the mass, stiffness, and damping at each location will be carried out.

Finally, the model will be validated against the experimental data used to identify it. It can be numerically simulated under conditions similar to those used to generate the clinical data and from the response of the simulated system natural frequencies and damping ratios may be

determined and compared to those obtained from the modal analysis of subject data. The model may be considered suitable if the differences in these values are within an acceptable range. It is anticipated the vibration data analysis and system identification techniques investigated in this research may become basis for reconstructing human models and tracking the quality of bone for a specific patient. Such a computational and analysis framework may be useful for monitoring bone related degradation and may contribute towards the development of osteological monitoring technology which is based on non-invasive vibration data obtained from a subject while performing regular tasks (running, walking etc.).

## 2. Modal Parameter Extraction and Statistical Analysis of Clinical Data

### 2.1 Subject Data

Experimental vibration response data for 179 test subjects was provided by the University of Cincinnati. Subjects were grouped into four blind groups based on bone-lead levels. The experiment performed to produce this data utilized five skin-mounted accelerometers secured with tape and a stationary force measurement platform. Subjects were instructed to strike the plate five times with each foot. The resultant output is a table of time-domain data sampled at 1000hz, expressing the axial accelerations of each of the five accelerometers, as well as the force measured by the force plate. A schematic of the sensor placement is shown in Figure 9.

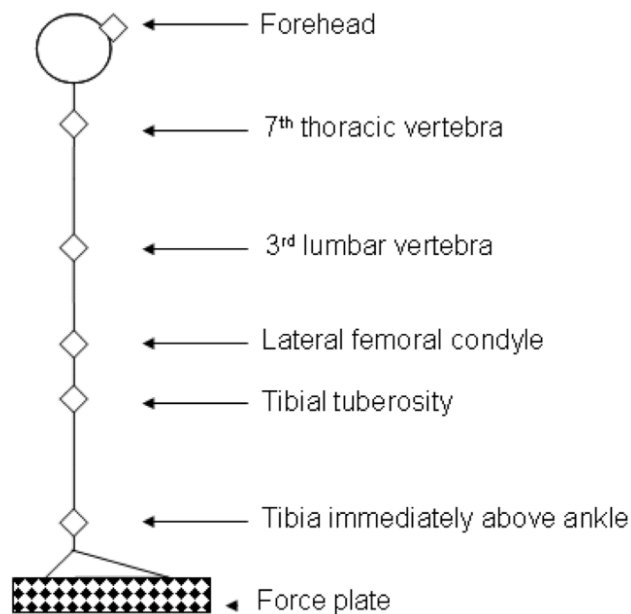


**Figure 9:** Schematic of accelerometer placement [38]

Only the data from the accelerometers placed on the lateral femoral condyle and tibial tuberosity on the striking leg are used in this analysis. The placement of these sensors as well as the force plate in relation to the skeletal structure are shown below in Figure 10. Note that in practice the sensors are mounted to the skin with adhesive tape, not attached directly to the bone. The skin and other soft tissues between the accelerometers and bone have been show to oscillate

at relatively low natural frequencies of less than 90 Hz, and exhibit much higher structural damping effects in comparison to bone [41].

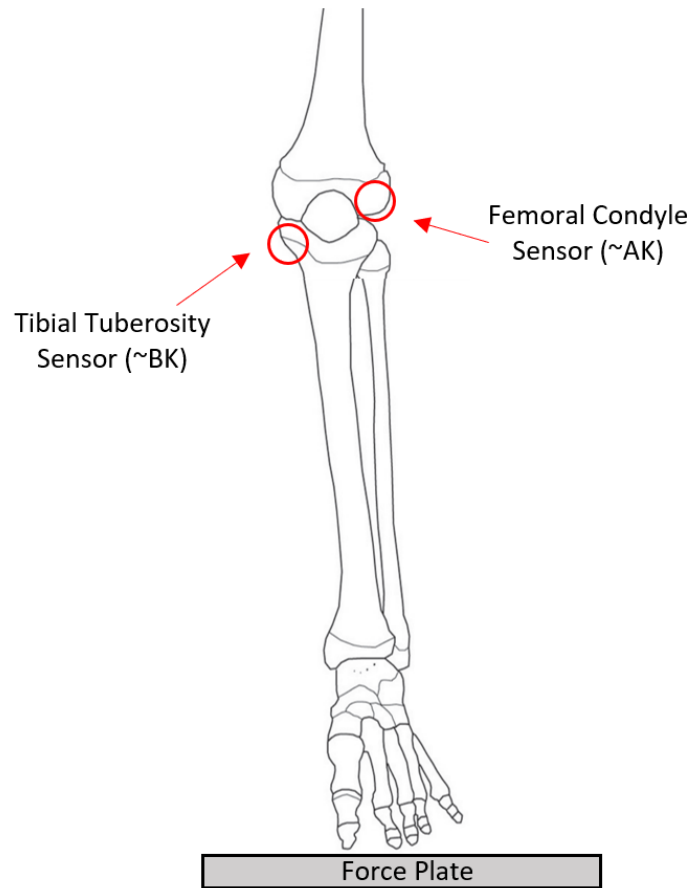


**Figure 10:** Sensor orientation in relation to skeleton

The next section describes the in-depth vibration modal analysis and statistical analysis of these data. This was done collaboratively with the research group of Dr. Bhattacharya at the University of Cincinnati. Rather than focusing on group-wise comparisons of subject data, the analysis below provides a basis for determining the grey-box model structure and developing validation criteria for the identified model. As the primary focus of the BSA metric is structural damping at specific modes, refining the damping ratios at the modes of interest is critical.

## 2.2 Frequency and Damping

Five time-domain tests were extracted from each subject data file. The arithmetic mean of the signals was used to create a single, clean time-domain vector for each sensor for conversion into the frequency domain. An example of the five tests and the mean is shown below in Figure 11.

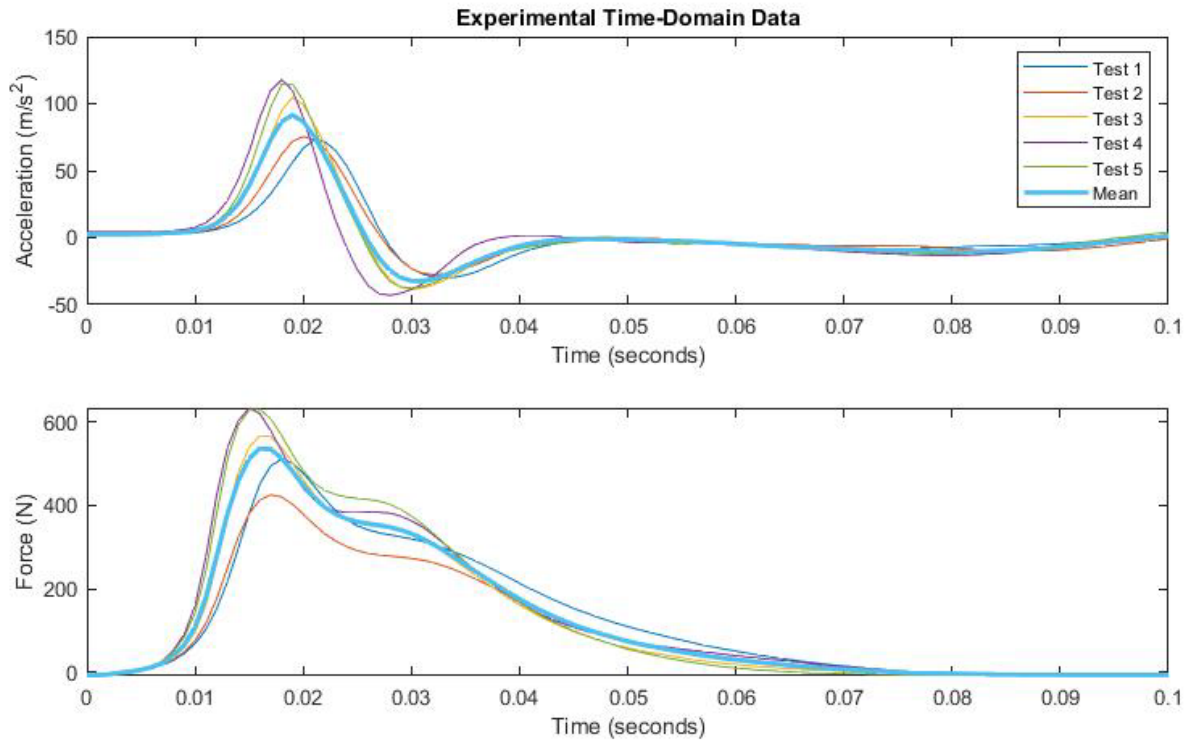


**Figure 11:** Characteristic time-domain signals from BSA experiment

The process described below was first applied to each of the five tests to determine three prominent modes for each. The means and standard deviations of the corresponding frequencies were calculated and used to validate the use of the averaged time domain signal, under the criterion that the frequencies identified from the averaged signal fall within one standard deviation of the mean of the individual tests. Averaging the time-domain signals proved valid, as demonstrated in Table 1.

**Table 1:** Validation of average time-domain signal

Frequency mean (Hz)	From Averaged Signals	valid
$36.27 \pm 3.64$	35.68	yes
$189.12 \pm 5.91$	185.54	yes
$466.65 \pm 2.36$	468.36	yes

To convert this discrete time-domain series into the frequency domain, the Laplace transform can be applied to the two signals,  $u(t)$  for the input force and  $\ddot{x}(t)$  for the output acceleration, via the relationship,

$$\mathfrak{T}\{\ddot{x}(t)\} = \ddot{X}(s) = \int_0^{\infty} \ddot{x}(t)e^{-st} dt \quad (2.1)$$

The FRF is then the transfer function evaluated along the frequency ( $j\omega$  axis) where  $s = j\omega$ , given by,

$$H(j\omega) = \frac{\ddot{X}(j\omega)}{F(j\omega)} = \text{Re}(H(j\omega)) + \text{Im}(H(j\omega)) = a(\omega) + jb(\omega) \quad (2.2)$$

The magnitude of the FRF, such as the one in Figure 12, can then be expressed as,

$$|H(j\omega)| = \sqrt{a^2(\omega) + b^2(\omega)} \quad (2.3)$$

The MATLAB Signal Processing Toolbox provides numeric methods to convert the time-domain force and acceleration data from the experiment into the frequency domain [42]. The *modalfrf* tool generates the frequency response function for the desired force plate/accelerometer combination using Welch's method. An example of such an FRF is shown in Figure 12 below. Natural, or resonant frequencies of the system are represented by peaks on the frequency response plot. This tool allows the computation of natural frequencies and corresponding damping ratios associated with a given modes of vibration. The flatter peaks represent modes with higher damping whereas the sharper peaks correspond to lower damping in the higher modes. It is important to highlight that in prior studies by Bhattacharya et. al. [38], damping ratio associated with the fundamental modes is correlated with the dynamic bone health quality indicators. In this study, understanding of the damping parameters associated with the higher modes are targeted, as shown in Figure 12 here.

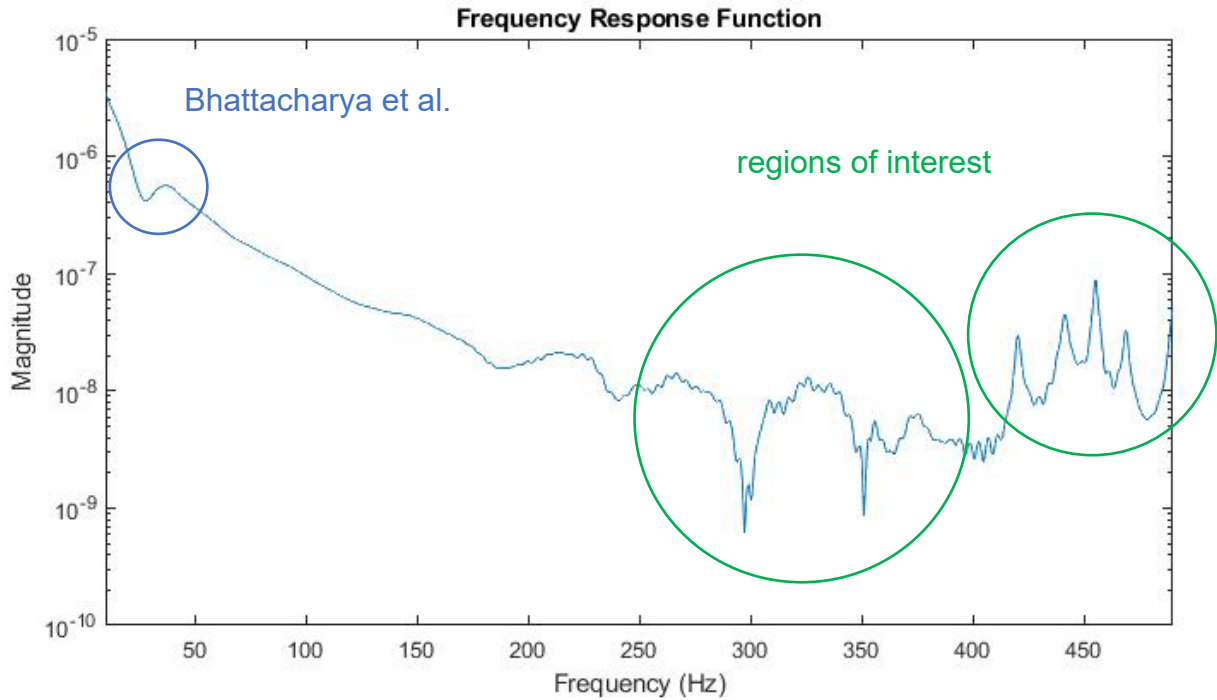


**Figure 12:** Example of a typical BSA FRF (10-250 Hz)

Each frequency response function for each sensor and subject was then separated into several smaller bins to better identify less prominent local peaks in each region. The *modalsd* command can be used to generate a produce a modal stabilization diagram to help determine the number of modes in a given frequency window. The columns of “+” and “o” markers represent regions of the curve that are stable in frequency and damping, and correlate to the real modes of the system. By counting the number of vertical lines formed by these markers, and initial estimate can be made for curve order. Stable modes are indicated on the FRF by the symbols explained in the legend of Figure 13.

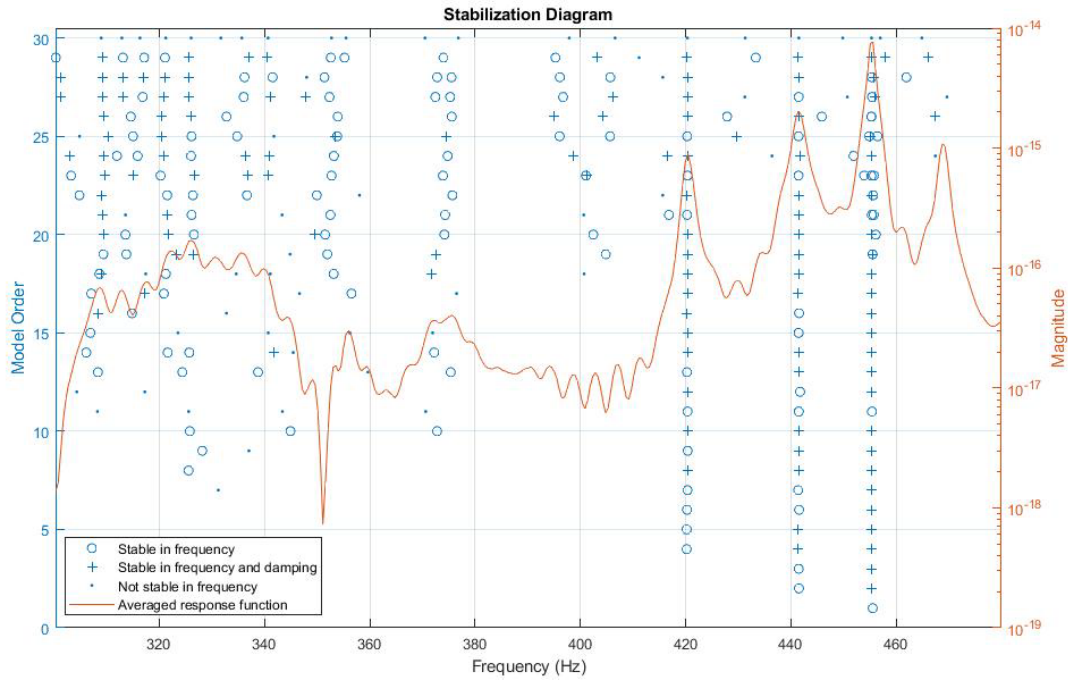


**Figure 13:** Modal stabilization diagram

To further clarify the number of modes identified from the modal stabilization diagram, the phase of the FRF can be plotted as well. Peaks on the diagram in Figure 14 also indicate the presence of vibrational modes.

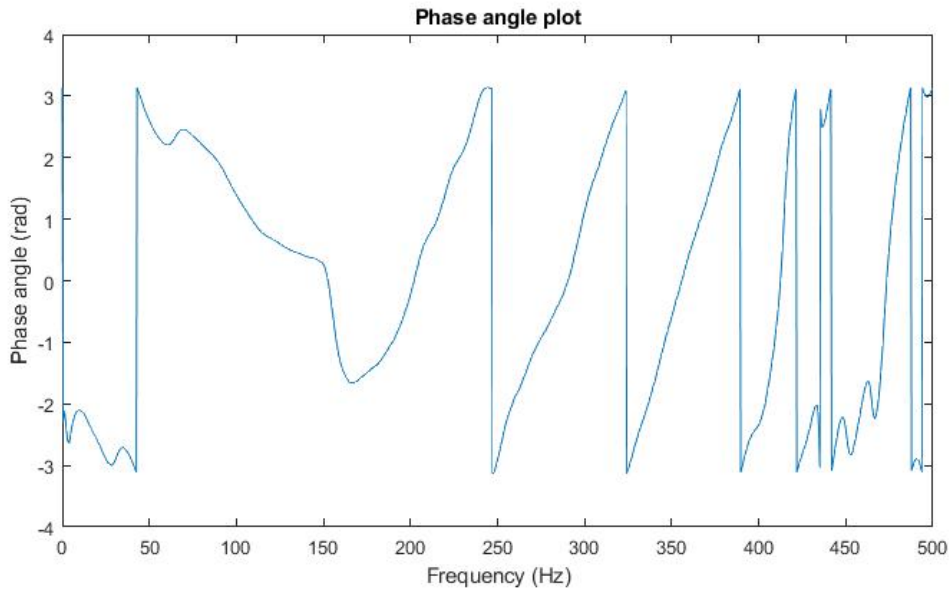


**Figure 14:** Phase angle plot for estimation of modes

The number of stable modes for each stabilization diagram was used to provide an initial estimate for identification of mode parameters via the rational fraction polynomial method [43]. This method takes an estimate for the number of modes to identify, to which the results are very sensitive. To best identify prominent modes and negate the effects of lost modes near bin edges, the analysis was performed twice using the different bin schemes shown in Figure 15. Table 2 below shows the classification of each frequency bin which are used for the analysis.

**Table 2:** Frequency bin ranges

	Set 1	Set 2
Bin 1	10 – 100 Hz	10 – 120 Hz
Bin 2	100 – 270 Hz	120 – 290 Hz
Bin 3	270 – 480 Hz	290 – 480 Hz

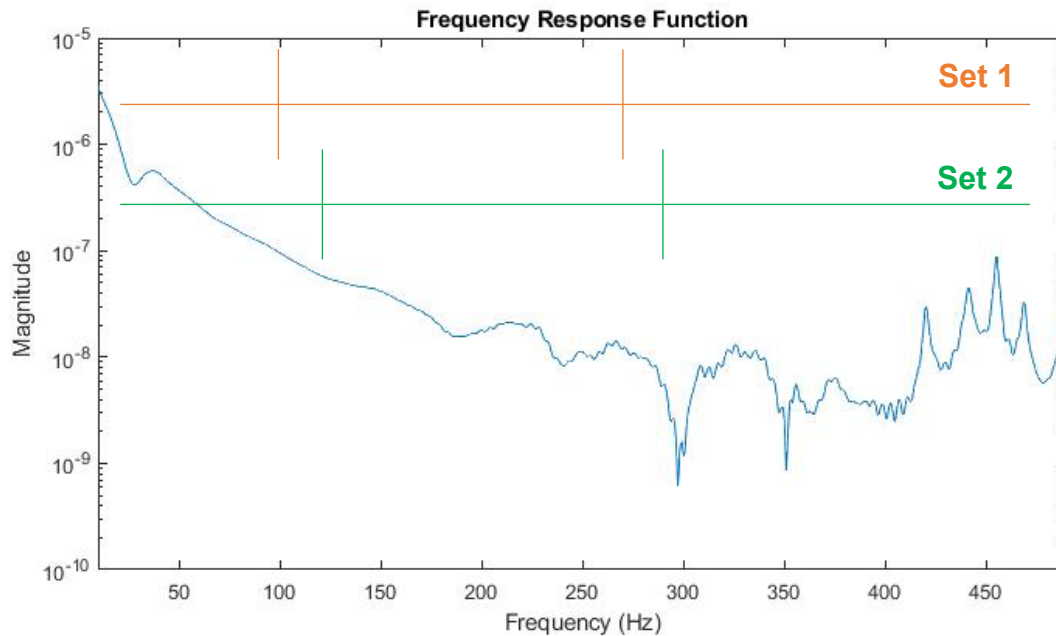


**Figure 15:** Frequency bin sets, graphical

These were optimized so that each bin is centered on a region containing prominent modes to avoid losses near bin edges. Each bin was then evaluated and fitted individually, with the curve

order specified and updated manually for each. An example curve fit is shown in Figure 16, indicating three clear modes between 420 Hz and 480 Hz.

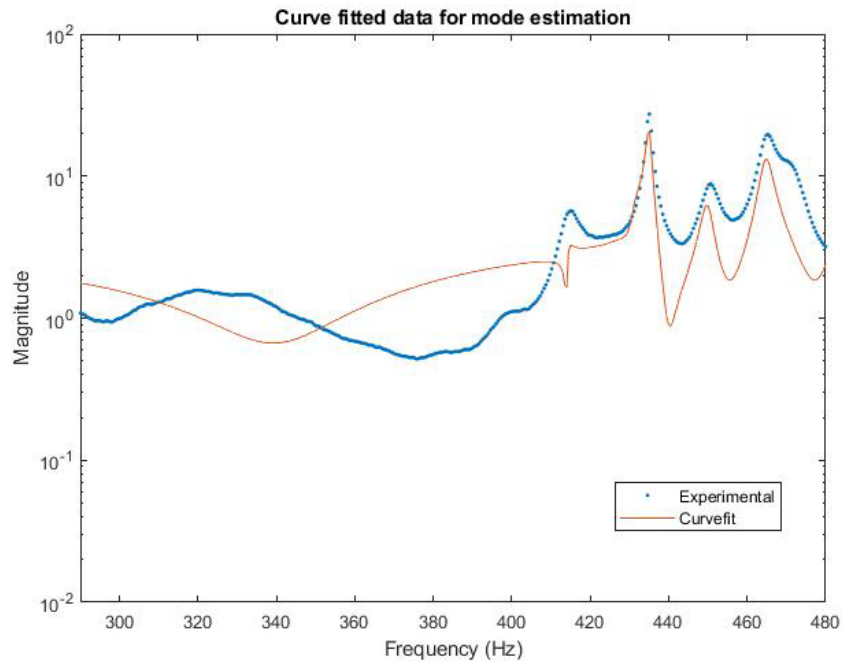


**Figure 16:** Curve fit for mode estimation of upper set 2 frequency range

The results of each observation were then combined by group and sensor for statistical analysis. The far extremes ( $<10$  Hz and  $>480$  Hz) were removed to negate the effects of singularities in these regions.

### 2.3 Preliminary Statistical Analysis

As evident in the sample frequency response function shown in Figures 8 and/or 9, an individual data set can have multiple peaks representing multiple vibration modes and their respective directions. In order to determine an appropriate model order for curve fitting, prominent frequencies must be identified. The estimated frequency-damping pairs from all test subjects were assembled into a single two-column matrix. Histograms of the estimated frequencies for both sensors are shown in Figure 17 with bin sizes of 10 Hz.

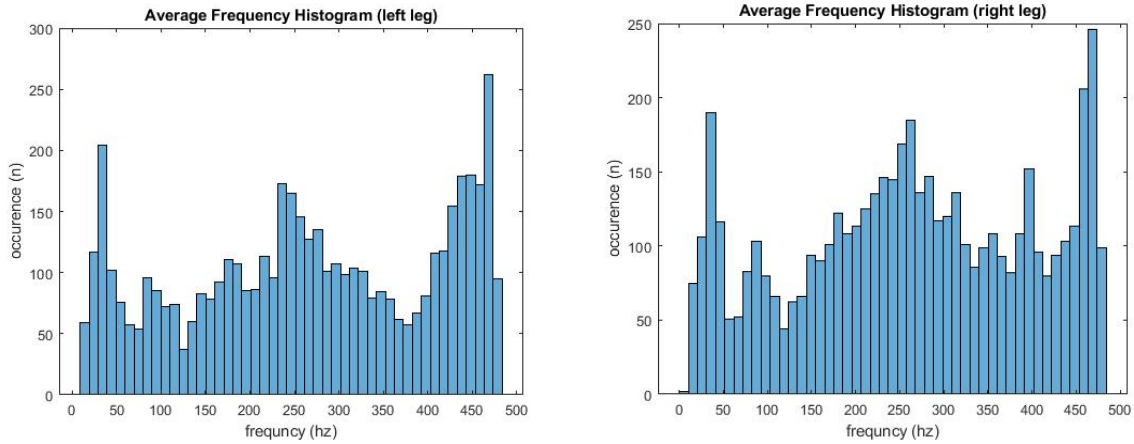


**Figure 17:** Frequency histograms for all subjects

Note that the overlapping estimation scheme employed results in prominent frequencies occurring up to twice as many times as less prominent frequencies. By removing all bins with an occurrence less than a certain threshold, bands containing prominent frequencies may be identified. Figure 18 below show the same histograms with all bins where  $n < \mu + \sigma$ . The three remaining bin sets in the regions of 40hz, 350hz, and 450hz suggest a model order of at least three.

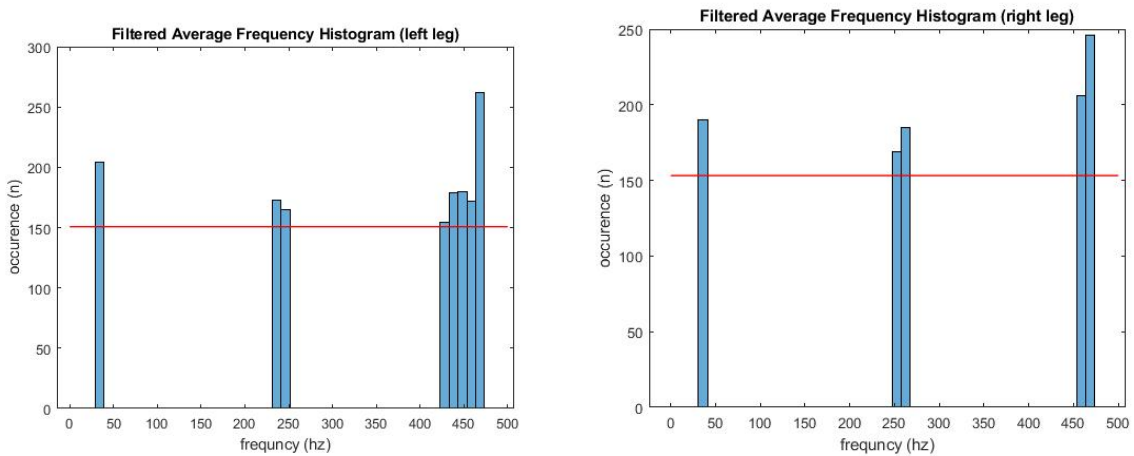


**Figure 18:** Filtered frequency histograms for all subjects

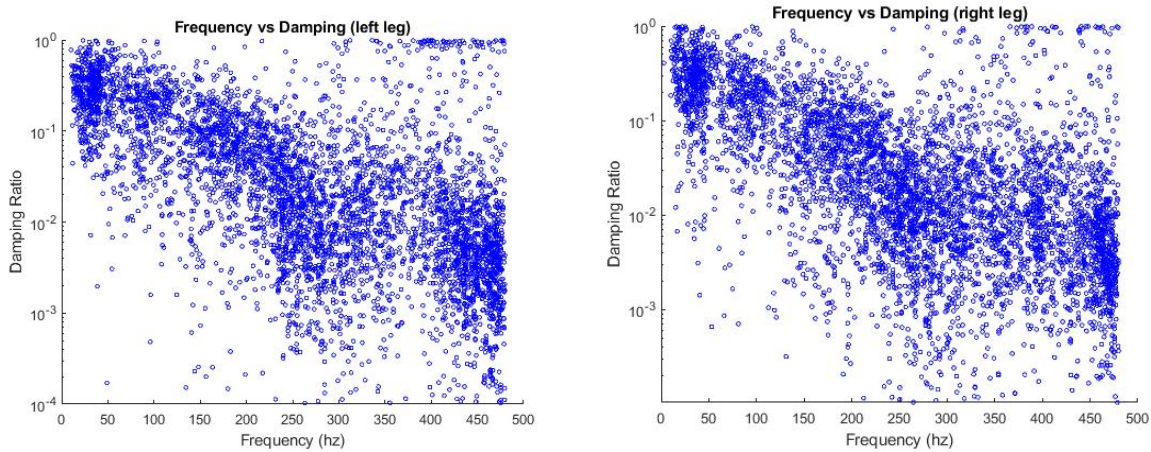


**Figure 19:** Scatter plots for all tests

The scatterplots of the estimated frequency-damping pairs in Figure 19 appear to show high density regions of points in the frequency ranges identified in the filtered histograms. Note that the damping ratios are plotted on a logarithmic scale to better show regions of high density. The peak in the frequency response function in Figure 12 and Figure 15 corresponding to the first mode is the only one typically identified in the range of 15hz – 100hz used to quantify bone quality in previous studies [38]. Also, note the relative prominence of the peaks in the higher frequency bands above 100 Hz., which is the target of this study.

## 2.4 *Density Based Spatial Clustering of Applications with Noise*

Identification of the frequency and damping ranges for each mode from these data is necessary to validate the proposed research described in later sections. Additionally, determination of the number of modes within the frequency range of 0-500hz is necessary to determine the appropriate order for a model representing the lower extremity.

The Density-Based Spatial Clustering of Applications with Noise (DBSCAN) provides a robust clustering method that does not require knowledge of the number of clusters and does not require the clusters to be of a specific shape. Additionally, this algorithm identifies data that do not belong to any of the clusters, allowing for simple rejection of outliers based on cluster assignment. DBSCAN works by identifying regions of a minimum density level separated by regions of lower density [44]. The frequency-damping pairs obtained from the FRFs are assigned

to clusters based on two parameters provided by the user, and based on the distribution of the data and the desired results of clustering, referred to as *epsilon* and *minPts*.

*MinPts* is defined by the user based on the desired results of the clustering analysis. This parameter defines the minimum number of sample points in each region that are required to classify that region as a cluster. This parameter must be at least  $n+1$ , where  $n$  is the number of dimensions of the input data. In most cases, *minPts* will be significantly larger than this minimum value. *Epsilon* can be considered an expression of desired “minimum density” for each region. This parameter is used as the search radius for neighboring points around each point of interest. Points must be within one *epsilon* of each other in a region containing at least *minPts* number of points to be classified as a cluster. These parameters may be modified iteratively to obtain desired results, however analysis of the distribution of the data set provide a good basis for selection of *epsilon* based on a user-defined *minPts* value [45].

## 2.5 Clustering Parameters

Calculation of the distance between the data points in each set provides a mathematical basis for selection of *epsilon*. The resulting matrix **D** can then be sorted in ascending order, resulting in a distribution similar to the example shown in Figure 20. The vertical axis represents the Euclidean distance between each point, while the horizontal axis expresses the indices of the sorted values. Note the sharp increase near the upper bound of the set. This “knee point” represents the position in **D** where the distances between points begin to rapidly diverge, and it provides a good upper estimate for *epsilon*. From here, *epsilon* may be decreased to refine the clusters under stricter criteria.

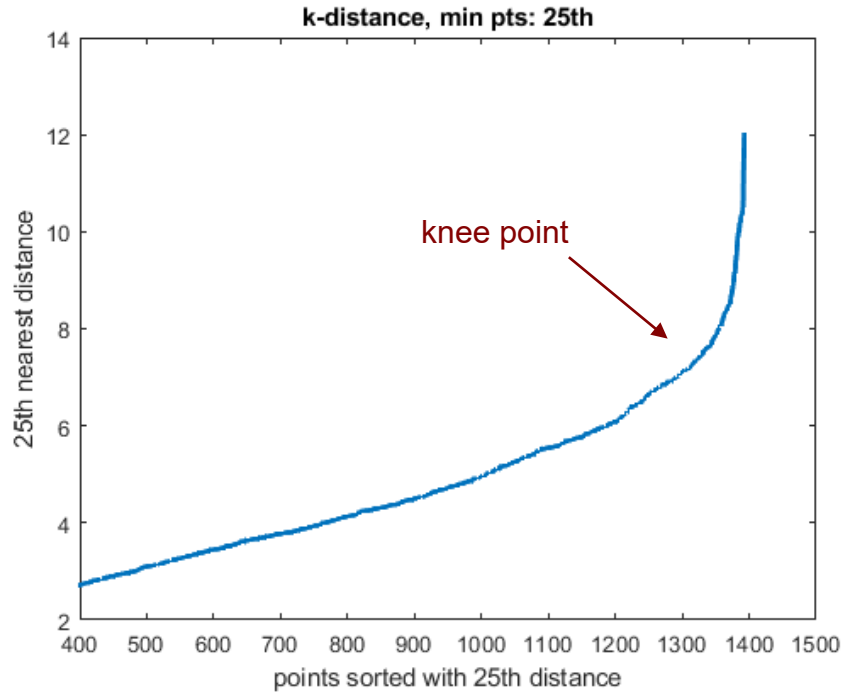


**Figure 20:** Example of a plot of sorted Euclidean distances

This knee point may be found by a numerical bisection method. At each step, a linear fit is performed on the points to the left of the bisection point as well as those to the right of the bisection points. The sum of squared errors between each of the fit and the bisection point is calculated at each step. The bisection point that minimizes the error curve is the knee point [46]. While this algorithm works well for smooth functions, it is sensitive to the small variations in the experimental data distribution. To improve performance, a 6<sup>th</sup> degree polynomial fit was first performed on the distance function, and the knee point algorithm was then applied to the fitted curve to determine an estimate for *epsilon*.

## 2.6 Implementation

DBSCAN was used to identify prominent frequency-damping pairs for each subject by grouping these pairs by bone-lead quartile and sensor. While DBSCAN will classify outliers as outside of any cluster, the algorithm is more effective when some preliminary cleaning is performed. Due to noise and error in the frequency-damping pair calculation, outliers must be

removed. These outliers were determined using the criteria shown below. These criteria were selected based on graphical analysis of scatterplots similar to those in Figure 19, as well as graphical iteration of the clustering algorithm. A 6<sup>th</sup> degree polynomial fit was performed to minimize the effect of the many local inflection points and capture only the knee point of interest. The degree of this fit was determined iteratively through trial and error.

Clustering was performed by first fixing a *minPts* value, approximately proportional to the group sizes. Identification of the knee point was implemented numerically in MATLAB for consistency. Recall that *epsilon* is an expression desired density in each region with at least *minPts* number of observations and may be modified to highlight different regions of the data set. The *y*-value at the knee point can be modified by introducing a factor *epmod* which may be iteratively modified to highlight the desired results. For example, for group 1 if *epmod* is made to be 1, the resulting clusters are too large for identification of the desired modes, shown in Figure 21. Non-clustered data is represented by red markers.

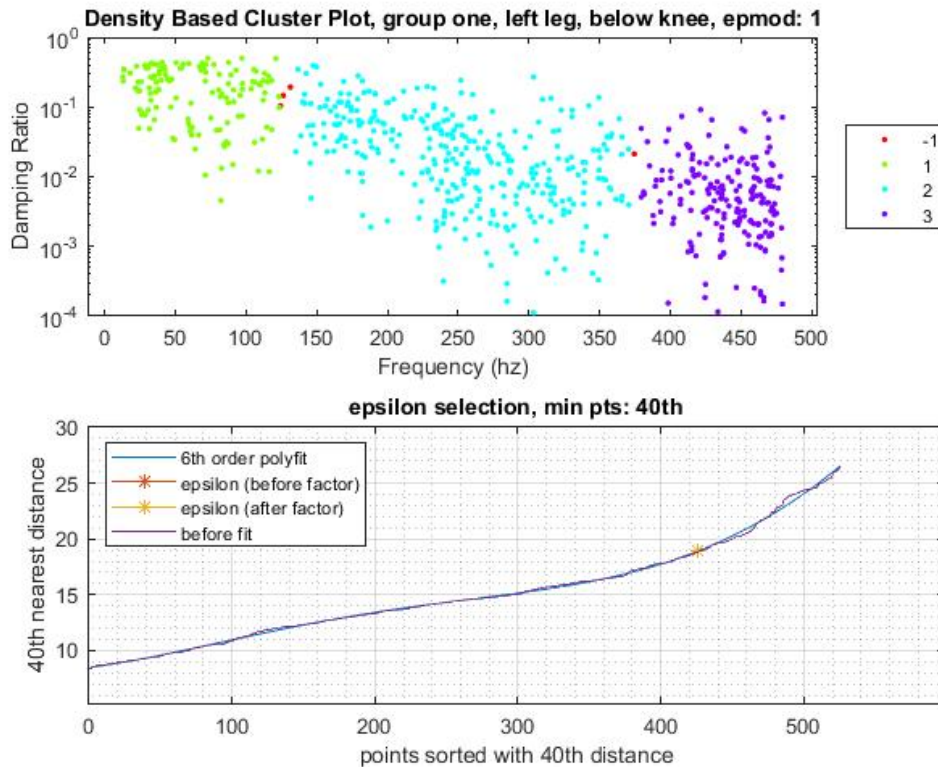


**Figure 21:** DBSCAN results with *epmod* = 1

If  $\epsilon$  is reduced too far, say to 0.4 shown in Figure 22, the point density criteria becomes too stringent, resulting in too many clusters in some regions and complete failure to generate clusters in others,

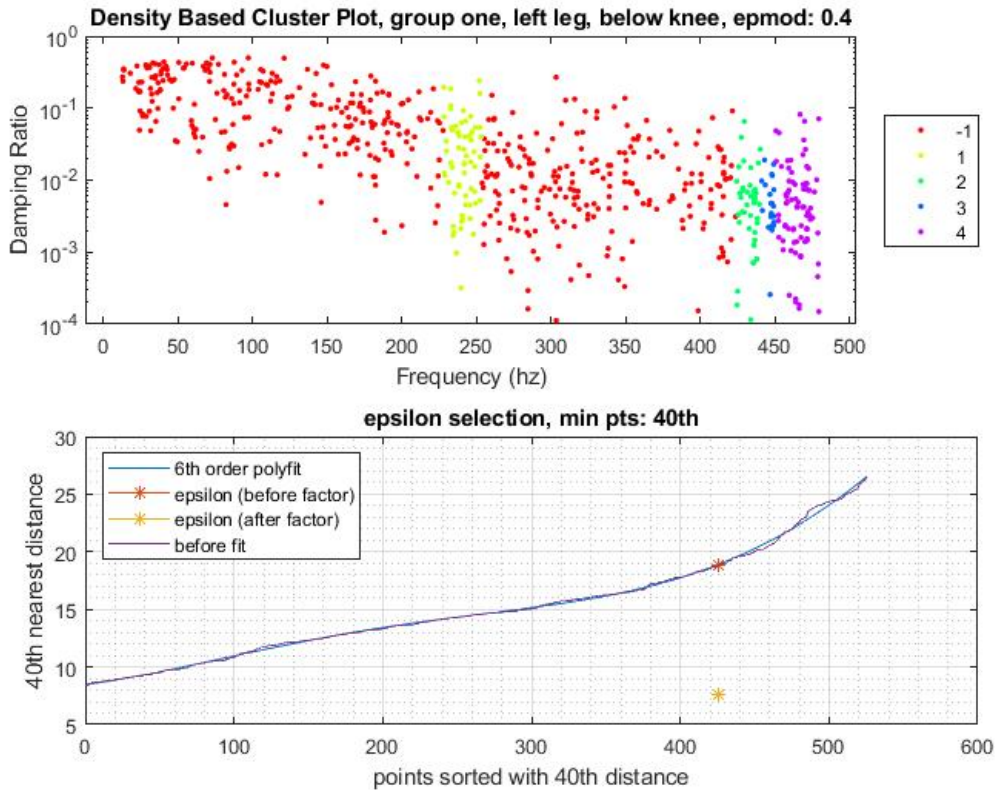


**Figure 22:** DBSCAN results with  $epmod = 0.4$

The goal for this process was to identify three distinct modes corresponding to the peaks in the histograms shown in Figure 17. For this data set, a satisfactory value for  $epmod$  was found to be 0.7, while data sets fell somewhere between 0.5 and 1. For some quartile/sensor groups,  $minPts$  had to be modified as well. Additionally, it was impossible to highlight only the three clusters of interest in some cases, so some figures may contain up to five clusters. Extra clusters were then removed manually.

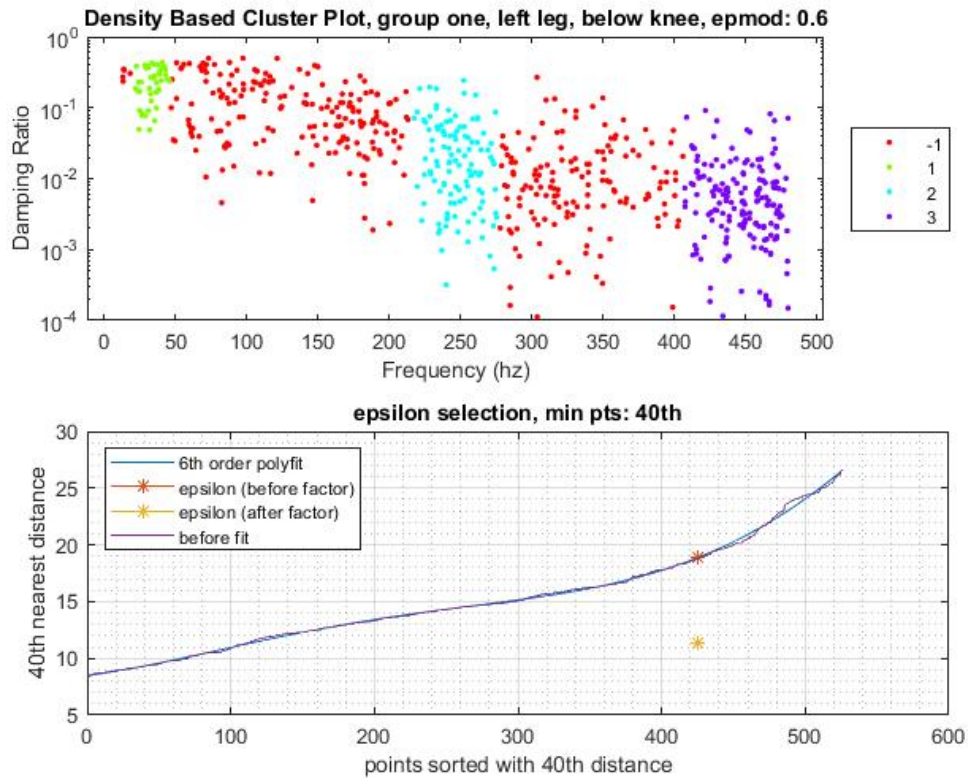


**Figure 23:** DBSCAN results for the below-knee sensor for quartile 1

Figure 23 above shows the results of the DBSCAN algorithm for the lateral femoral condyle sensor data from subject in the first lead quartile, as well as the k-distance plot and epsilon before and after multiplication by *epmod*. The tables provided below contain the mean and standard deviation of damping ratios associated with each set of observations for each sensor in the respective groups.

**Table 3:** First Mode: ~30hz

	Group 1	Group 2	Group 3	Group 4
LAK	0.2732 ± 0.1262	0.2805 ± 0.1254	0.2558 ± 0.1199	0.273 ± 0.1145
LBK	0.2364 ± 0.1181	0.2202 ± 0.0982	0.2133 ± 0.1065	0.258 ± 0.1421
RAK	0.2753 ± 0.1163	0.2423 ± 0.1303	0.2338 ± 0.1137	0.3021 ± 0.1186
RBK	0.2189 ± 0.1334	0.2065 ± 0.1163	0.2029 ± 0.1222	0.2322 ± 0.1404

**Table 4:** Second Mode: ~250hz

	Group 1	Group 2	Group 3	Group 4
LAK	0.0312 ± 0.0382	0.0318 ± 0.0433	0.0289 ± 0.0407	0.0317 ± 0.0345
LBK	0.0339 ± 0.0447	0.0421 ± 0.0568	0.0231 ± 0.0292	0.0222 ± 0.0325
RAK	0.0363 ± 0.0442	0.0202 ± 0.0287	0.0208 ± 0.0238	0.0207 ± 0.0306
RBK	0.0333 ± 0.0429	0.0256 ± 0.0367	0.022 ± 0.0231	0.0325 ± 0.0422

**Table 5:** Third Mode: ~450hz

	Group 1	Group 2	Group 3	Group 4
LAK	0.0083 ± 0.0132	0.0096 ± 0.0139	0.0059 ± 0.0087	0.0079 ± 0.0129
LBK	0.0096 ± 0.015	0.0103 ± 0.0156	0.0063 ± 0.0069	0.0085 ± 0.0128
RAK	0.0075 ± 0.0095	0.008 ± 0.0118	0.006 ± 0.007	0.0111 ± 0.0189
RBK	0.0061 ± 0.0094	0.0081 ± 0.0109	0.0078 ± 0.0105	0.0073 ± 0.0083

Cluster analysis via DBSCAN was able to identify three prominent modes of interest for each combination of sensor and group at approximately 30hz, 250hz, and 450hz. There is an apparent decreasing trend across all damping values corresponding to an increase in mode frequency. This trend was quantified by a one-way analysis of variance (ANOVA) between the low and high frequency modes for each group and sensor [47]. Figure 24 and Figure 25 below show the results of ANOVA for the sensor mounted on the tibial tuberosity of Group 1 subjects. The p-values for each of these ANOVA analyses are on the order of  $10^{-33}$ , demonstrating a significant difference between damping values for each pairing. This suggests that higher frequencies and their damping ratios may be associated with stiffer bone/muscle groups of lower extremities and may serve as a better indicator for bone health quality.

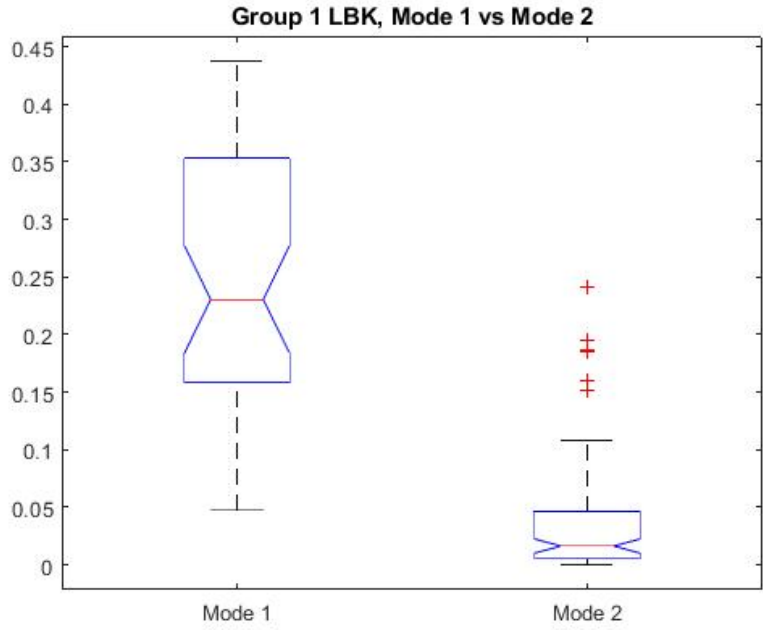


**Figure 24:** ANOVA of Modes 1 and 2 for Group 1 LBK

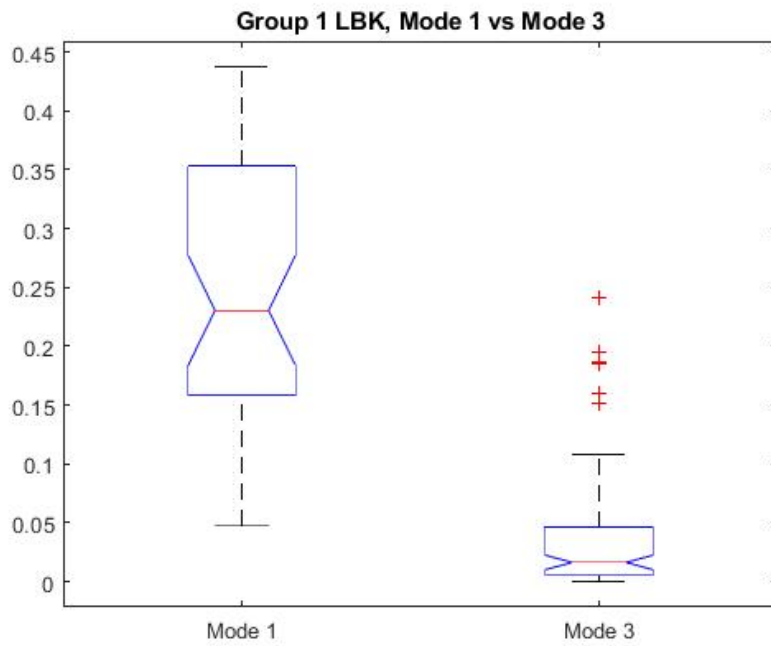


**Figure 25:** ANOVA of Modes 1 and 3 for Group 1 LBK

## 2.7 Bin-Based Mode Criteria

In order to establish a basis of comparison between groups, the cluster data generated by DBSCAN was used to fix the boundaries of frequency range bins corresponding to each mode. This was accomplished by taking the weighted means of the highest and lowest values in each cluster. This was done first across the groups, yielding bin boundary estimates for each sensor. These boundaries were again averaged to obtain three sets of boundaries, one corresponding to each mode.

For each sensor and mode combination, the following formula was applied to both the lower and upper edges of the cluster to obtain a two-element vector  $\bar{B}$  containing the average upper bound and lower bound across all four groups.  $\bar{b}_i$  refers to each bin boundary, and  $n_i$  refers to the number of observations in each bin set.

$$\bar{B} = \frac{\bar{b}_1 n_1 + \bar{b}_2 n_2 + \bar{b}_3 n_3 + \bar{b}_4 n_4}{n_1 + n_2 + n_3 + n_4} \quad (2.4)$$

This provides several expected ranges for observations of each mode depending on the placement of the accelerometer of the patient's skin. These ranges are shown in Table 6, Table 7 and Table 8 respectively.

**Table 6:** Global bin boundaries for Mode 1, by sensor

	LBK	LAK	RBK	RAK
lower	18.40	19.37	22.31	26.10
upper	47.78	43.16	49.89	47.08

**Table 7:** Global bin boundaries for Mode 2, by sensor

	LBK	LAK	RBK	RAK
lower	218.82	216.34	193.43	219.82
upper	286.30	277.00	308.44	283.84

**Table 8:** Global bin boundaries for Mode 3, by sensor

	LBK	LAK	RBK	RAK
lower	403.74	415.51	289.39	443.24
upper	479.16	478.93	478.80	478.22

Global criteria for mode estimation can be obtained from these results as well. The maxima, minima, and averages of the boundaries within each mode provide loose, stringent, and moderate criteria for classifying the observations respectively. The averages, once again normalized by number of observations, are shown in Table 9 below.

**Table 9:** Means of each sensor boundaries, by mode

	Mode 1a	Mode 2a	Mode 3a
	21.48733822	210.1688499	394.2338351
	47.10377045	291.0250204	478.8535536

Each observation was then reclassified by these frequency criteria rather than clustering. The tables below contain the means and standard deviations of the damping ratios for each group/sensor combination.

**Table 10:** First Mode: ~30hz

	Group 1	Group 2	Group 3	Group 4
LAK	0.2507 ± 0.1399	0.2764 ± 0.0335	0.2462 ± 0.1125	0.2633 ± 0.1151
LBK	0.2333 ± 0.0085	0.2292 ± 0.0918	0.0983 ± 0.1095	0.2483 ± 0.1426
RAK	0.2585 ± 0.1216	0.2358 ± 0.1330	0.2338 ± 0.1137	0.3127 ± 0.01159
RBK	0.2222 ± 0.1344	0.2094 ± 0.1157	0.2005 ± 0.1227	0.2231 ± 0.1412

**Table 11:** Second Mode: ~250hz

	Group 1	Group 2	Group 3	Group 4
LAK	0.0314 ± 0.0398	0.0312 ± 0.0436	0.0299 ± 0.0397	0.0296 ± 0.0383
LBK	0.0321 ± 0.0433	0.0433 ± 0.0579	0.0289 ± 0.0340	0.0294 ± 0.0440
RAK	0.0351 ± 0.0428	0.0244 ± 0.0340	0.0269 ± 0.0341	0.0249 ± 0.0360
RBK	0.0334 ± 0.0435	0.0266 ± 0.0391	0.0242 ± 0.0315	0.0239 ± 0.0314

**Table 12:** Third Mode: ~450hz

	Group 1	Group 2	Group 3	Group 4
LAK	0.0100 ± 0.0159	0.0105 ± 0.0159	0.0073 ± 0.0108	0.0090 ± 0.0141
LBK	0.0097 ± 0.0145	0.0105 ± 0.0155	0.0065 ± 0.0072	0.0085 ± 0.0128
RAK	0.0106 ± 0.0145	0.0084 ± 0.0119	0.0080 ± 0.0113	0.0127 ± 0.0187
RBK	0.0101 ± 0.0140	0.0123 ± 0.0153	0.0100 ± 0.0137	0.0111 ± 0.0155

Several conclusions may be drawn from these preliminary findings. For all groups, there is a decrease in damping ratio corresponding to an increase in frequency, consistent with the trend observed in the scatter plots in Figure 19, and possibly representing better capturing of bone dynamics at higher frequencies. Additionally, there appears to be a decrease in damping ratio corresponding to an increase in group number, where group one is the healthy control group and group four is the group with the highest blood-lead level. In the next section this decrease will be statistically tested.

## 2.8 *Group-wise Analysis of Variance*

To test the hypothesis that a decrease in the damping factor correlates to a decrease in bone quality, and by extension an increase in bone-lead levels, the mean damping values at each mode were compared by repeated group-wise one-way analysis of variance. This was conducted independently at each of the four sensor locations: above the right knee, below the right knee,

above the left knee, and below the left knee. A statistically significant difference in the mean damping values was demonstrated for some, but not all of the combinations. This was first performed for the results from the clustered data, and the p-values for each pair are shown in Table 13, Table 14, Table 15, and Table 16. Pairs with a p-value less than 0.05, corresponding to a confidence interval of 95% are highlighted.

**Table 13: LBK cluster ANOVA**

Mode	1 vs 2	1 vs 3	1 vs 4	2 vs 3	2 vs 4	3 vs 4
1	0.4769	0.3402	0.4309	0.7469	0.1293	0.0903
2	0.2202	0.0457	0.0303	0.0036	0.0019	0.8486
3	0.689	0.0175	0.4626	0.0063	0.2653	0.0682

**Table 14: LAK cluster ANOVA**

Mode	1 vs 2	1 vs 3	1 vs 4	2 vs 3	2 vs 4	3 vs 4
1	0.7976	0.5191	0.9948	0.3356	0.7774	0.4929
2	0.9035	0.6665	0.9198	0.5856	0.9834	0.604
3	0.4003	0.0882	0.8283	0.0097	0.2915	0.1398

**Table 15: RBK cluster ANOVA**

Mode	1 vs 2	1 vs 3	1 vs 4	2 vs 3	2 vs 4	3 vs 4
1	0.8416	0.5264	0.628	0.4088	0.7704	0.2873
2	0.0097	0.0142	0.8474	0.0001	0.0015	0.0167
3	0.0001	0.2746	0.3891	0.0002	0.0002	0.7827

**Table 16: RAK cluster ANOVA**

Mode	1 vs 2	1 vs 3	1 vs 4	2 vs 3	2 vs 4	3 vs 4
1	0.2469	0.0912	0.2868	0.7586	0.0394	0.0065
2	0.0001	0.0015	0.001	0.8793	0.9106	0.976
3	0.7729	0.2249	0.0807	0.2131	0.2383	0.0294

This was the performed again for the data for the damping values determined by the frequency bin criteria outlined in chapter 2. The p-values are again shown below in Table 17, Table 18, Table 19, and Table 20.

**Table 17: LBK bin ANOVA**

Mode	1 vs 2	1 vs 3	1 vs 4	2 vs 3	2 vs 4	3 vs 4
1	0.8677	0.1493	0.5932	0.1818	0.4952	0.0649
2	0.0793	0.4986	0.6097	0.0171	0.0373	0.9241
3	0.6263	0.0169	0.4247	0.005	0.2167	0.0996

**Table 18: LAK bin ANOVA**

Mode	1 vs 2	1 vs 3	1 vs 4	2 vs 3	2 vs 4	3 vs 4
1	0.4113	0.8737	0.6432	0.2956	0.6406	0.4947
2	0.9566	0.7427	0.6821	0.8056	0.7503	0.9456
3	0.8209	0.0787	0.5323	0.0482	0.3996	0.238

**Table 19: RBK bin ANOVA**

Mode	1 vs 2	1 vs 3	1 vs 4	2 vs 3	2 vs 4	3 vs 4
1	0.6159	0.4014	0.9774	0.7247	0.6289	0.4325
2	0.1473	0.0343	0.0273	0.5689	0.5137	0.9276
3	0.1842	0.9481	0.5400	0.1843	0.5292	0.5197

**Table 20:** RAK bin ANOVA

Mode	1 vs 2	1 vs 3	1 vs 4	2 vs 3	2 vs 4	3 vs 4
1	0.4164	0.3285	0.0372	0.9415	0.0053	0.0016
2	0.0158	0.0618	0.0212	0.5395	0.9033	0.6291
3	0.1589	0.0894	0.2632	0.7705	0.0244	0.0128

While the bin-based mode criteria provide a faster and more generalized method for determining prominent subject modes, it is not as robust as the density-based clustering method. Across each group, the DBSCAN method resulted in 21 pairs of damping values with a demonstrably significant difference, while the bin-based criteria identified only 14. While statistical significance was not demonstrated for all pairings, in those with a demonstrated difference the p-values at the two higher frequency modes were generally smaller than those at the lower frequency mode, and mean damping ratios trended downward for the groups with higher blood-lead levels, supporting the hypothesis. For instance, consider the comparison between the damping ratios at mode 2 for group 1 and group 4 at the left below-knee sensor, shown in Figure 26 below. This is from the cluster-based criteria.

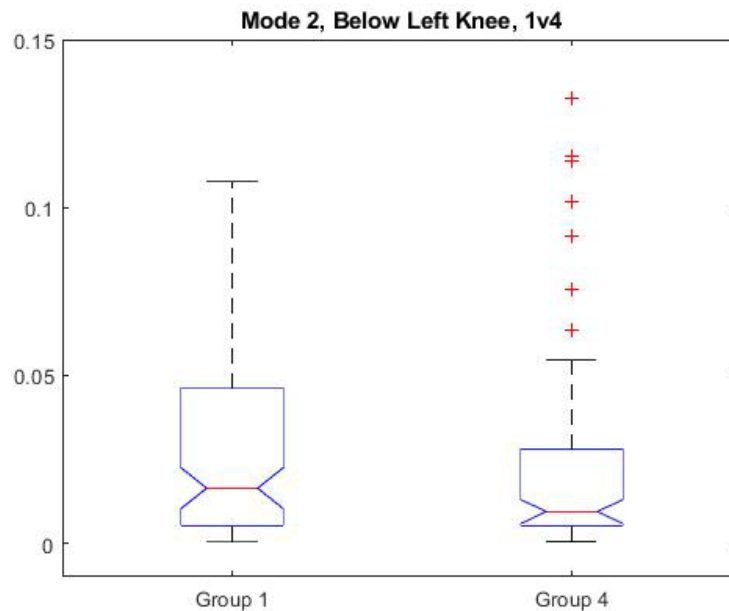


**Figure 26:** Groupwise ANOVA example, Mode 2, LBK, 1 vs 4

From group 1 (lowest blood-lead) to group 4 (highest blood lead) there is a 0.0117 decrease in the damping ratio, with a p-value of 0.0142, indicating a statistically significant difference between the measurements. Future experiments should seek to improve the quality of all damping measurements to determine if such a difference exists for all comparisons. Measurements taken from the above-knee sensors proved somewhat more effective than those from the below-knee sensors, while curiously, the quality of the results seems to vary depending on which leg is chosen for the test, with the right leg providing better results. While this may be explained by the fact that roughly 81% of the human population is right-leg dominant, it is also likely that it represents inconsistencies in the experimental measurements or analysis [48]. Potential ways to improve the quality of measurement and analysis are explored in section 4.2.

## **2.9    *Limitations and Improvements***

Despite its resistance to noise and ability to identify clusters of arbitrary shape, differences in data distribution and sample sizes necessitate iterative modification of *epsilon* and *minPts*. The current method requires a researcher to manually test different values, which, when coupled with the relatively long runtime for the MATLAB and lack of a reactive GUI, makes this method time consuming and difficult to implement. A graphical toolbox, shown in Figure 27, was created specifically for this task as a demonstration on how this process could be significantly streamlined. This application makes use of the DBSCAN package for R developed by Hahsler et. al [49].

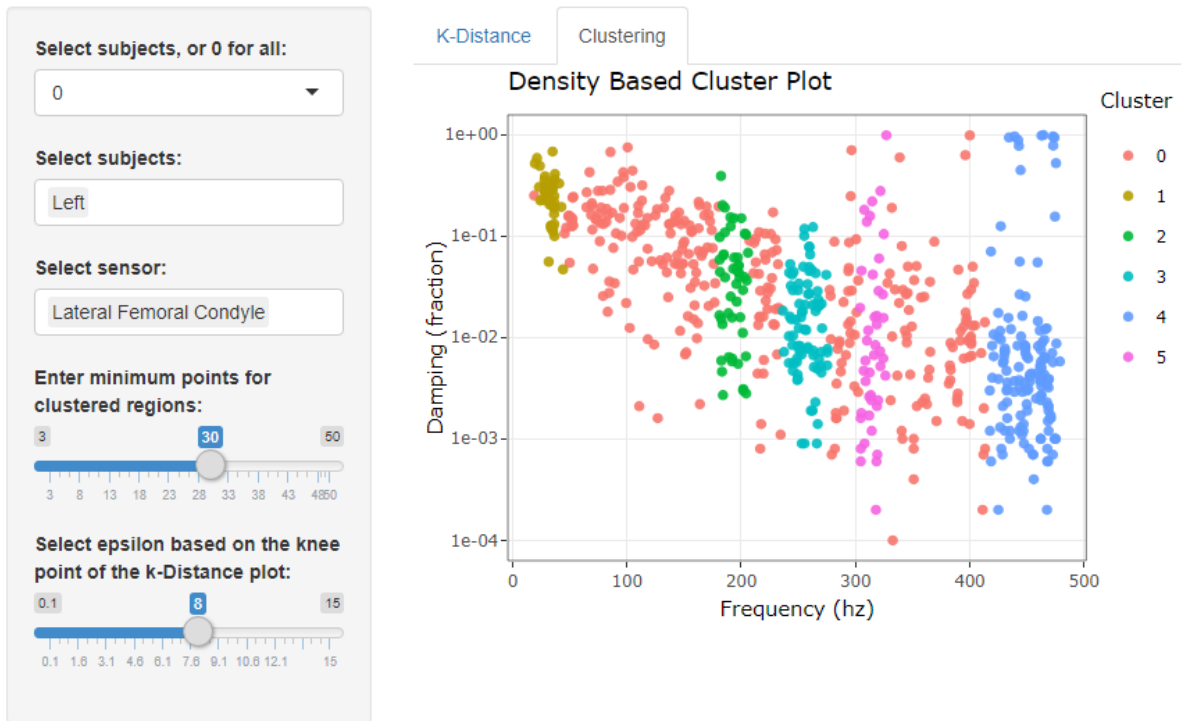


**Figure 27:** Demonstration of graphical BSA toolbox

The application allows the user to select subject groups and modify *epsilon* and *minPts* to generate the k-distance plot and clustering results simultaneously, as well as allowing for reactive, real time updating of the parameters. A .csv file containing the clustering data can then be generated and exported. Hovering the cursor over each point display information. In the future, an additional tab could be added to the application to also provide statistical information on each cluster as well, containing the means, standard deviations, and pair-wise ANOVAs for each group combination.

### 3. Development of A System Identification Model

#### 3.1 Background

System identification describes a broad set of methods used to construct a model of a system using input-output data obtained experimentally, instead of constructing parametric models from known parameters. Models constructed via system identification offer robust ecological validity, as they can account for phenomena not totally described by physical laws [50]. The addition of certain assumptions, for instance ensuring a non-negative mass, helps to refine and improve the speed of system identification methods. Models for which no details about the structure of the system are known are called black-box models. Grey box models presuppose certain constraints as well as the model order [51].

#### 3.2 Basic Algorithms

The MATLAB System Identification Toolbox provides tools to estimate model parameters for a variety of input-output data types [52]. For grey box models, four estimation algorithms are available. For this analysis, the Levenberg-Marquardt least squares search is used, which is a combination of gradient descent and Gauss-Newton Methods. These algorithms seek to iteratively reduce the cost function, which represents the sum of the squares of the residuals and is given by,

$$F = \frac{1}{2} \sum_{i=1}^m (\varepsilon_i(y, y'))^2 \quad (3.1)$$

where  $m$  is the total number of observations.  $F$  is the vector of residuals and the error  $\varepsilon_i$  of each iteration is given by,

$$\varepsilon_i(y, y') = \frac{1}{2} (y - y')^2 \quad (3.2)$$

$y'$  is the estimated value, and  $y$  is the actual value of the cost function. The following algorithms describe methods for minimizing  $\varepsilon(x)$ , which is an expression of error between the fit and the actual values.

### 3.3 Simple Batch Gradient Descent Method

The gradient descent method aims to compute the local minimum of the objective function at each point  $x$ . A starting point is chosen, then a guess for a line tangent to the data is made. Consider a linear polynomial function with unknown parameters  $a$  and  $b$ ,

$$y' = ax + b \quad (3.3)$$

$$\theta = [a, b] \quad (3.4)$$

$\theta$  refers to a vector of the unknown parameters, or weights, to be estimated and updated on each iteration. Recall that the gradient of a function is a two-dimensional vector field expressing the directional derivative of the function. Let  $h$  be the “descent direction” which is the downhill direction of the gradient. The gradient can be computed as the change in the cost function with respect to the weights and represents a downhill trend in the residuals of the function. The weights are updated iteratively to find values for unknown parameters  $a$  and  $b$  that minimize the error. The gradient is computed as,

$$\frac{\partial \varepsilon}{\partial \theta} = \left[ \frac{\partial \varepsilon}{\partial a}, \frac{\partial \varepsilon}{\partial b} \right]. \quad (3.5)$$

In this case,

$$\frac{\partial \varepsilon}{\partial a} = \frac{2}{N} \sum_{i=1}^N -X(Y - aX + b), \quad (3.6)$$

and,

$$\frac{\partial \varepsilon}{\partial b} = \frac{2}{N} \sum_{i=1}^N -(Y - (aY + b)), \quad (3.7)$$

where  $X$  and  $Y$  are the observed data points at the current position. The value of  $\theta$  is then updated as follows,

$$\theta_i = \theta_{i-1} - r \frac{\partial \varepsilon}{\partial \theta} \quad (3.8)$$

until the parameter estimate converges ( $r \rightarrow 0$ ). The learning rate  $r$  is the step size of each iteration. A small  $r$  is precise at the cost of estimation speed. A large  $r$  means fewer iterations and results in a faster estimation but reduces precision. The error for each point is to be combined into total cost function described above.

Let us consider the linear first-order algorithm described above and define a set of data points with a normal noise distribution,  $X$  and  $Y$ . Let's also define a vector  $\theta$  containing an arbitrary guess for the slope and y-intercept,  $a$  and  $b$  respectively. The algorithm described above was implemented in MATLAB with  $r=0.01$  and  $iterations=100$ . A set of random data points were generated to approximately follow an arbitrary line, and the fit algorithm was applied to identify the governing parameters. The estimated curve along with different iteration results are shown in Figure 28 demonstrating the convergence of the algorithm at  $a=3.8766$  and  $b=0.87658$ .

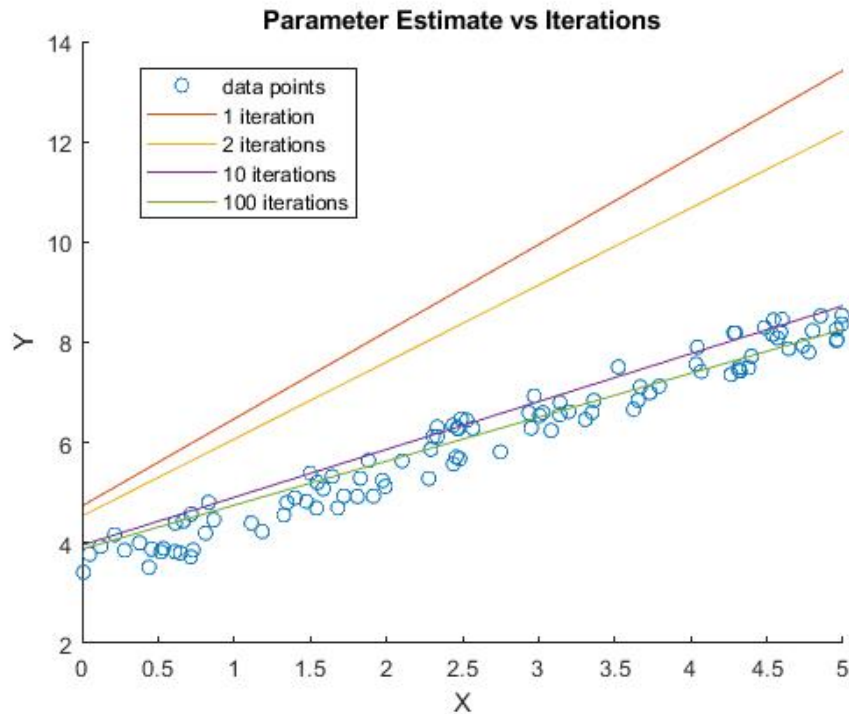


**Figure 28:** Linear gradient descent example

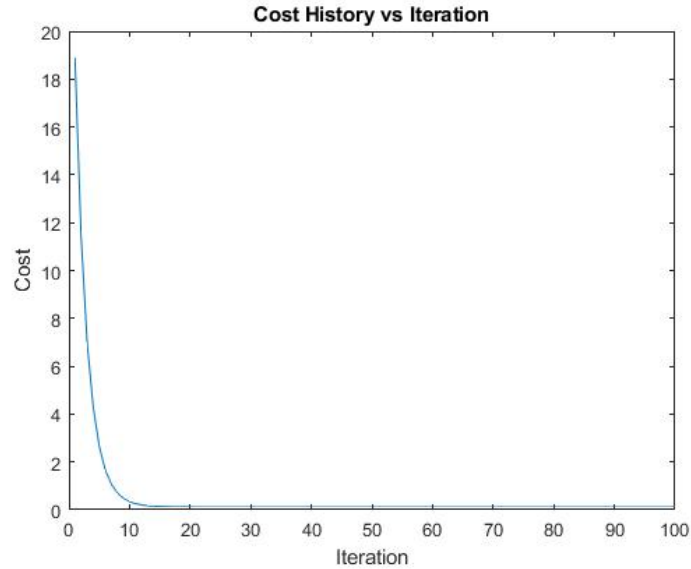


**Figure 29:** Changes in the cost function with each iteration

Note in Figure 29 convergence of the cost function is shown highlighting that around iteration 30 the cost reaches its minimum. Similar algorithms may be applied to any order of curve fit by increasing the number of unknown parameters of higher order polynomials. For example, let us now consider the quadratic polynomial,

$$y' = ax^2 + bx + c \quad (3.9)$$

The error function now becomes,

$$F(x) = \frac{1}{N} \sum_{i=1}^N (Y - (aX^2 + bX + c))^2 \quad (3.10)$$

As model order is increased, computing the gradient becomes increasingly difficult and gradient calculation may be impossible if the derivative approaches zero. Another inherent drawback of this method is that accurate estimations necessitate a small  $r$ , increasing computation time. While methods exist to automatically optimize  $r$ , it is typically set manually by the user. Long runtime is exacerbated if the initial estimates for  $a$  and  $b$  are far from the convergent values. Furthermore, for higher order models, the complexity and runtime of this algorithm is substantially increased.

### 3.4 Gauss Newton Method

For identification of nonlinear systems, other methods are more efficient than the simple batch gradient descent in estimating function parameters. The Gauss-Newton method serves as the basis for a variety of other methods, and functions by approximating a non-linear differential equation as a series of linear approximations, which can then each be solved iteratively. The Gauss-Newton algorithm follows the following steps [53].

1. Choose an initial  $x$  in the subspace  $\mathbb{R}^n$
2.  $J^T J h_k = -J^T f(x_k)$  is solved for  $h_k$
3. Set  $x_{k+1} = x_k + h_k$
4. Iterate steps 3 and 4 until convergence

$J$  is the Jacobian matrix containing the first partial derivatives, and is computed by,

$$((J(x))_{ij} = \frac{\partial f_i}{\partial x_j}(x) \tag{3.11}$$

Convergence of the Gauss-Newton method is not guaranteed, and the algorithm fails if  $J$  is singular, as the descent direction  $h_k$  becomes undefined. Other methods modify the Gauss-Newton method to minimize or negate its inherent drawbacks.

### 3.5 Levenberg-Marquardt

The Levenberg-Marquardt method is similar to the Gauss-Newton method but adds a damping term  $\mu$  in the manner shown below.

$$(J^T J + \mu I)h = -J^T f(x) \tag{3.12}$$

For all  $\mu > 0$ , the coefficient matrix  $(J^T J + \mu I)$  will be positive definite, ensuring a solution for  $h_k$  and guaranteeing convergence of the algorithm. The damping constant is modified on each iteration to increase efficiency. By increasing  $\mu$ , the step size is shortened, and the approximation moves towards the steepest descent direction. By decreasing  $\mu$ , the step size of the Levenberg-

Marquardt method is increased, decreasing runtime, and approaching an approximation similar to that generated by the Gauss-Newton method. The Levenberg-Marquardt method is faster than the Gauss-Newton method and enforces convergence [53].

### 3.6 System Identification Process and Factors influencing Identification Quality

To demonstrate the identification process and investigate the quality of the estimated parameters, the system identification process is first carried out here with simulated data based on the model by Kim et. al [34,35]. This three degree of freedom model structure is shown in Figure 30.

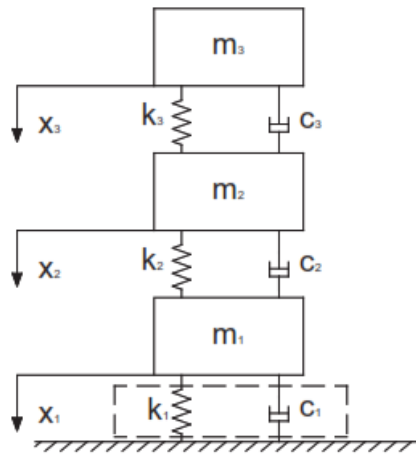


**Figure 30:** Kim et. al model [34,35]

To test the system identification process, this model is simulated with an impulse excitation applied at  $m_1$ . To remain consistent with the human model proposed in the subsequent section, the effect of gravity is ignored and the vibration about its static equilibrium position is considered. This results in the following differential system of equations in a slight change to the force matrix, shown below.

$$\underbrace{\begin{bmatrix} m_1 & 0 & 0 \\ 0 & m_2 & 0 \\ 0 & 0 & m_3 \end{bmatrix}}_{\mathbf{M}} \underbrace{\begin{pmatrix} \ddot{x}_1 \\ \ddot{x}_2 \\ \ddot{x}_3 \end{pmatrix}}_{\ddot{\mathbf{x}}} + \underbrace{\begin{bmatrix} c_1 + c_2 & -c_2 & 0 \\ -c_2 & c_2 + c_3 & -c_3 \\ 0 & -c_3 & c_3 \end{bmatrix}}_{\mathbf{C}} \underbrace{\begin{pmatrix} \dot{x}_1 \\ \dot{x}_2 \\ \dot{x}_3 \end{pmatrix}}_{\dot{\mathbf{x}}} + \underbrace{\begin{bmatrix} k_1 + k_2 & -k_2 & 0 \\ -k_2 & k_2 + k_3 & -k_3 \\ 0 & -k_3 & k_3 \end{bmatrix}}_{\mathbf{K}} \underbrace{\begin{pmatrix} x_1 \\ x_2 \\ x_3 \end{pmatrix}}_{\mathbf{x}} = \underbrace{\begin{bmatrix} -1 \\ 0 \\ 0 \end{bmatrix}}_{\mathbf{b}} f(t) \quad (3.13)$$

The parameters for this model are taken from [34,35] and are shown in Table 21 below.

**Table 21:** Kim model parameters [34,35]

Index	Mass (kg)	Stiffness (kN/m)	Damping (kNs/m)
1	1.12	0.05	0.17
2	3.26	94.10	0.44
3	50.62	40.10	0.04

First order realization of higher order differential equation associated with the  $n$ -degree of freedom model (3.13) can be represented by two state variables,  $x$  (displacement) and  $\dot{x}$  (velocity). The general state-space representation is as follows:

$$\begin{aligned} (\dot{\mathbf{z}})_{2n \times 1} &= [\mathbf{A}]_{2n \times 2n} (\mathbf{z})_{2n \times 1} + [\mathbf{B}]_{2n \times 1} (\mathbf{u})_{1 \times 1} \\ (\mathbf{y})_{m \times 1} &= [\mathbf{C}]_{m \times 2n} (\mathbf{z})_{2n \times 1} + [\mathbf{D}]_{m \times 1} (\mathbf{u})_{1 \times 1} \end{aligned} \quad (3.14)$$

where,  $\mathbf{A}$  is state matrix,  $\mathbf{z} = (\mathbf{x} \quad \dot{\mathbf{x}})^T$  is the state vector,  $\mathbf{B}$  is the input matrix,  $\mathbf{u}$  is input vector,  $\mathbf{y}$  is the output vector,  $\mathbf{C}$  is the output matrix, and  $\mathbf{D}$  is the direct feed-through matrix which represents the direct influence of the inputs on the outputs. The state matrix  $\mathbf{A}$  of the following form was formulated to allow for numerical simulation and estimation of the system.

$$\mathbf{A} = \begin{bmatrix} \mathbf{0} & \mathbf{I} \\ -\mathbf{M}^{-1}\mathbf{K} & -\mathbf{M}^{-1}\mathbf{C} \end{bmatrix} \quad (3.15)$$

The input matrix  $\mathbf{B}$  was created to apply the input force at the bottommost mass,  $m_3$ .

$$\mathbf{B} = \begin{bmatrix} \mathbf{0}_{3 \times 1} \\ \mathbf{M}^{-1}\mathbf{F} \end{bmatrix} \quad (3.16)$$

For displacement and velocity outputs at each mass, the output matrix then takes the form,

$$\mathbf{C} = \mathbf{I}_{m \times 2n} \quad (3.17)$$

For this model, there are  $3(n)$  degrees of freedom, and  $6(m)$  output states, resulting in a  $6 \times 6$  output matrix. To identify the model parameters, the System Identification Toolbox in MATLAB is used. The identification algorithm requires the output response at all degrees of freedom for any given input.

The resulting state space model, associated with (3.13) is then simulated with an impulse excitation of 100 N for the first 0.1 seconds, yielding the responses shown in Figure 31 below which are used as the output channels for identification. To provide the grey-box structure for identification, a function must be created consistent with the state space model. The initial estimates of the mass elements, stiffness elements, and damping constants are provided as input parameters for the system matrices  $\mathbf{M}$ ,  $\mathbf{C}$ , and  $\mathbf{K}$ , which define the state space system required for identification process. The model function and input parameters are provided as input arguments to the *idgrey* function, which generates a linear grey box model. The time-domain simulated data, input impulse force data and state responses, is passed to *greyest* function that implements the system identification process. The estimation algorithm (Gauss-Newton, Gradient Descent, or Levenberg-Marquardt) may be selected using *greyestOptions*, or set to “auto”, which allows MATLAB to select the algorithm that best minimizes the cost function. In all the examples presented in this study, this argument is set to “auto”, which typically results in selection of the Levenberg-Marquardt algorithm. The identification process also allows constraints to be applied for each input parameter and acceptable bounds for each parameter can also be selected for estimation.

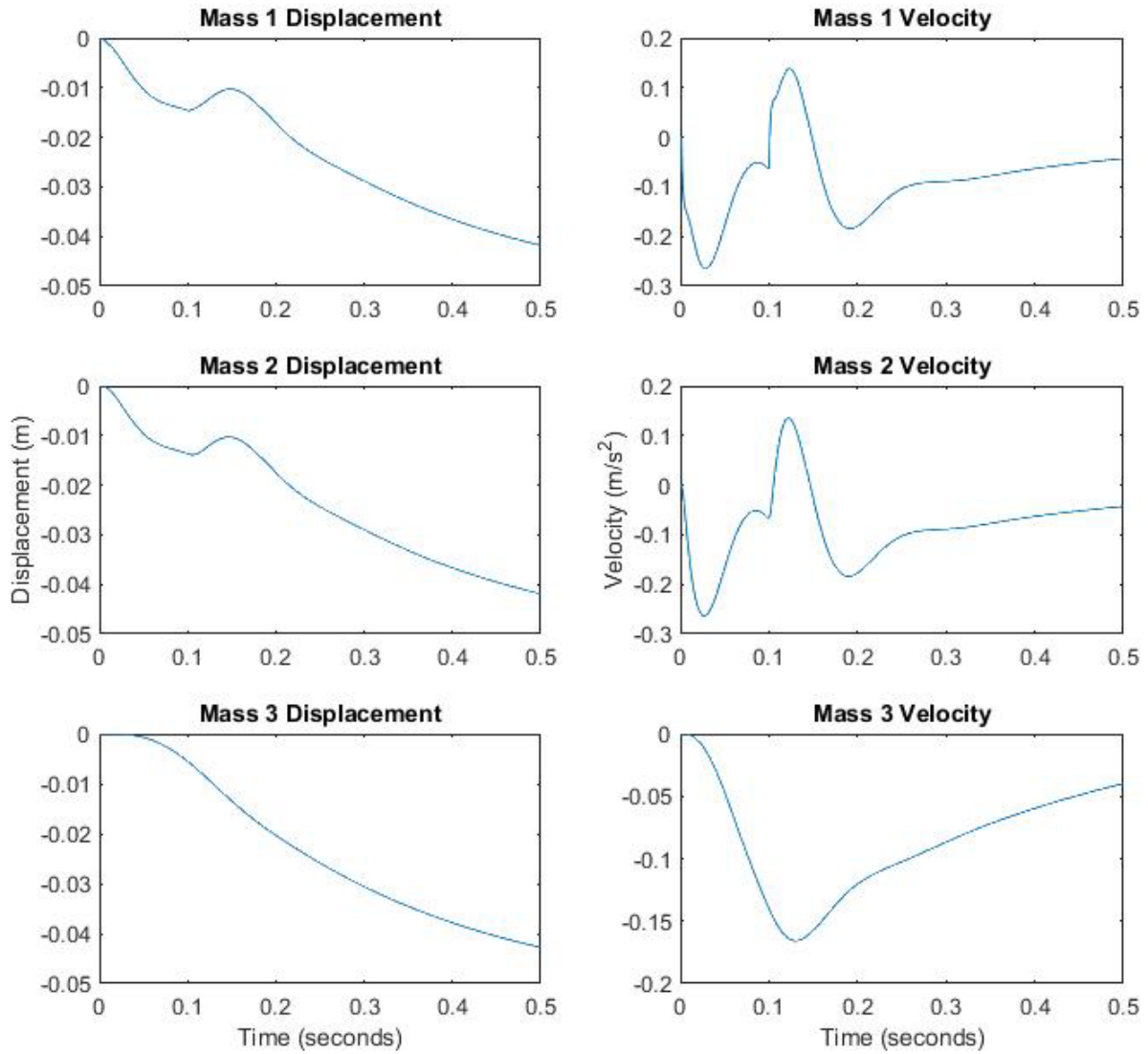


**Figure 31:** Simulated Kim model with 100 N / 0.1 s impulse

System identification can then be used re-estimate the model parameters in  $\mathbf{M}$ ,  $\mathbf{C}$ , and  $\mathbf{K}$  from the input and output signals. The grey-box model tools in the MATLAB System Identification Toolbox require initial estimates and ranges (constraints) for the parameters of the system. For this demonstration, the exact values of these parameters are known, as they were used to generate the input-output data, therefore using these values would result in perfect identification after the first iteration. Validation of the identification process therefore requires initial parameters that are different from the exact parameters. For these tests, each exact value for  $k$  and  $c$  was multiplied by a random number between 0.5 and 1.5 to obtain a different, randomized initial value.

The system identification was then run with fixed mass parameters and free, estimable stiffness and damping parameters. This was performed with all six output states (3 displacement and 3 velocity), and again with just the displacement states. In both cases, the quality of the estimate, quantified by the normalized root-mean-square error, was 100% for all channels. The displacement responses are shown in Figure 32 below. The initial, estimated, and actual system parameters are shown in Table 22.

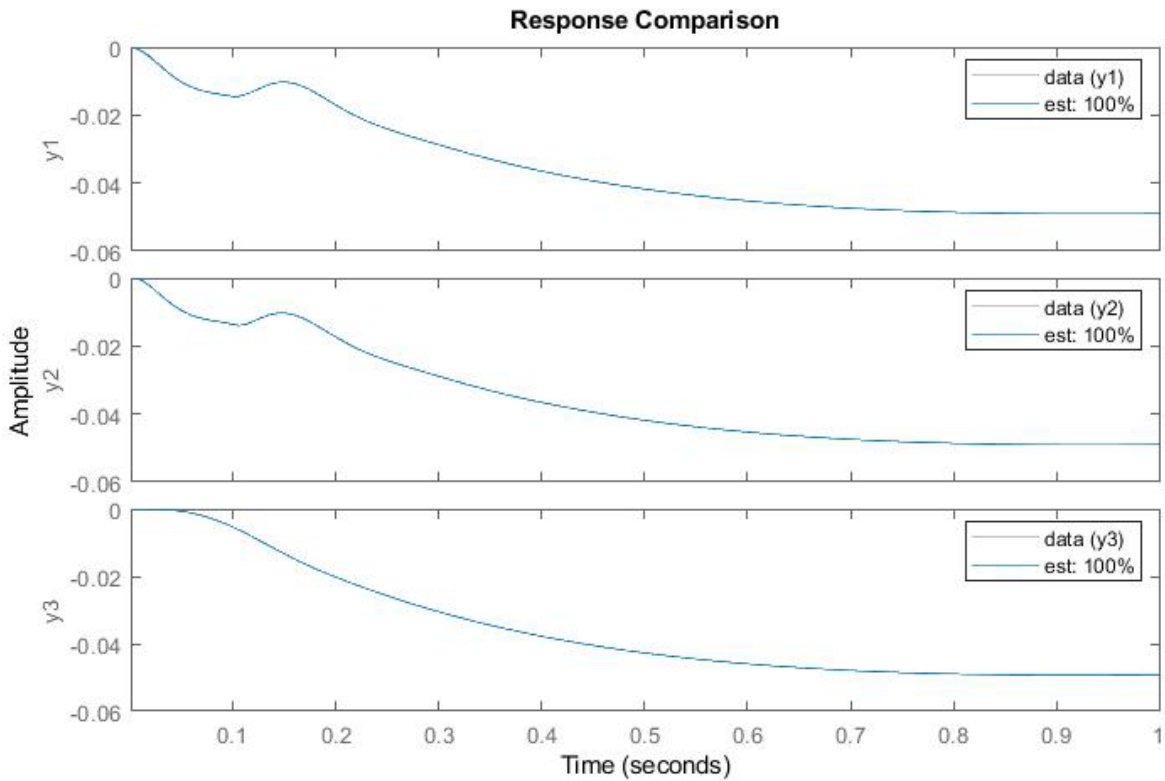


**Figure 32:** Displacement channels for re-identified system

While the identification quality of the simulated system is excellent, that was to be expected. Real, physical systems contain noise that results in inherent decreases in estimation quality. Normally distributed random noise with an amplitude of 1mm, when applied to the same simulated responses, resulted in a decrease in estimation quality for each channel of around 7%, demonstrated in Figure 33 below. The initial parameters were also randomized in this case.

**Table 22:** Parameters for re-identified system

Parameter	Initial Value	Estimated Value	Exact Value
$k_1$	539.19	50	50
$k_2$	$1.16 \times 10^5$	$9.41 \times 10^4$	$9.41 \times 10^4$
$k_3$	$1.16 \times 10^4$	$1.01 \times 10^4$	$1.01 \times 10^4$
$c_1$	172.76	170.00	170.00
$c_2$	262.61	440.00	440.00
$c_3$	26.47	40.00	40.00

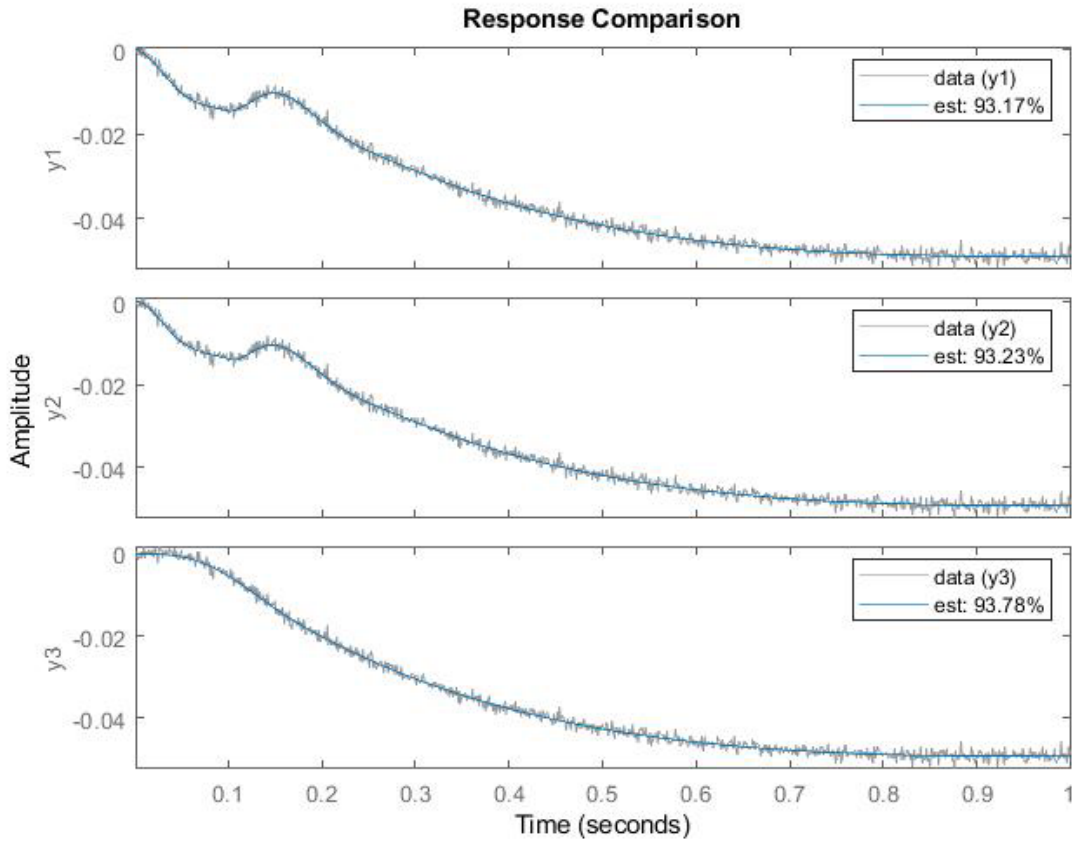


**Figure 33:** Identified displacement channels with random noise

These estimations are based on data obtained from a simulated model with a known structure. In real-world application however, system identification methods are used to identify

models using data obtained from experiments, which means that some assumptions must be made about an unknown model, for instance the proportional damping assumption described in the subsequent sections. This assumption was applied to the grey-box model structure used for identification, while the input-output data were the same as described above – generated using discrete, non-proportional damping elements. Again, the initial values were randomized, however no signal noise was added. Figure 34 below shows the result of this estimation, resulting in a further decrease in estimation quality.

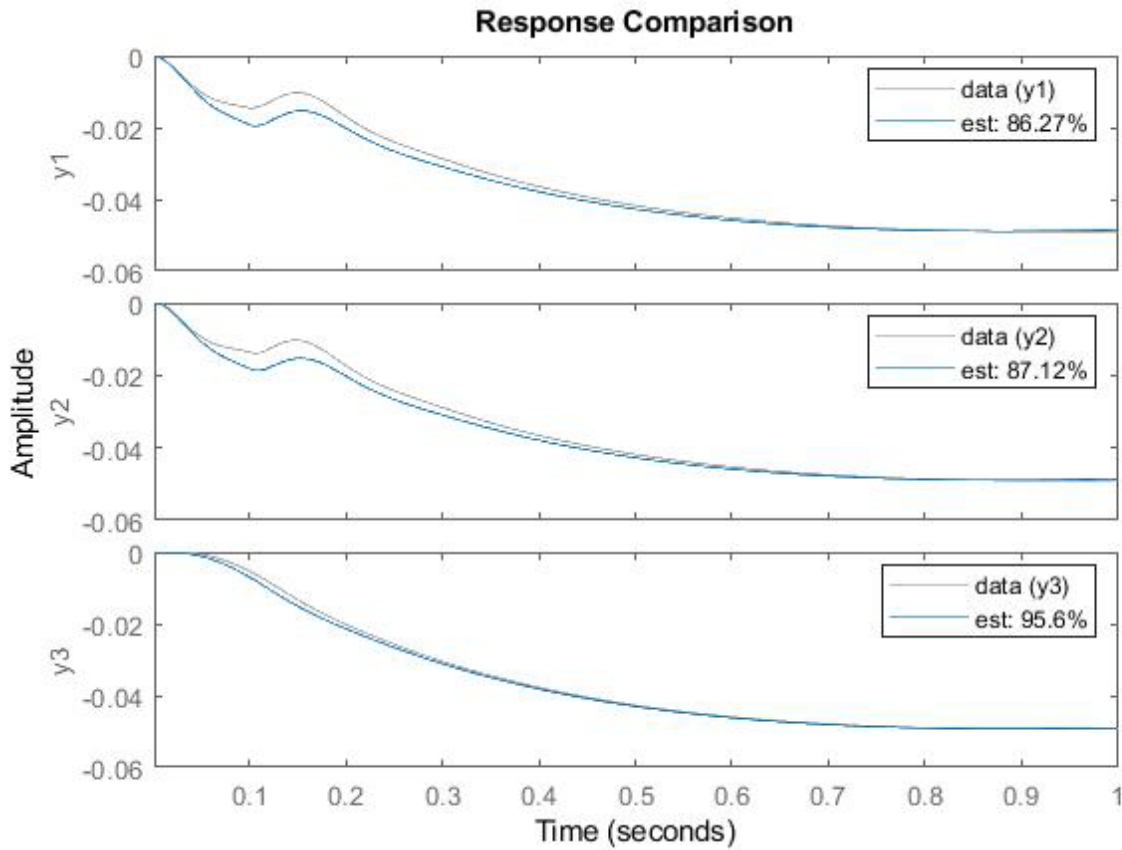


**Figure 34:** Effects of proportional damping assumption on estimation

For this example, the response of the system is known at all degrees of freedom, while another real-world limitation may be a missing sensor at one of the channels, as is the case with the data which will be used for the estimation of the human model in Section 3.7. In addition to system identification tools, the MATLAB System Identification Toolbox contains a function, *misdata*, that iteratively estimates missing data, which may be either gaps in a channel or a channel

simply not present [52]. The example in Figure 35 below shows the effects of estimated missing data at  $m_1$ , the lowermost mass at which the input force is applied. Again, the initial parameters are randomized, however the signal noise and proportional damping assumption are not applied.

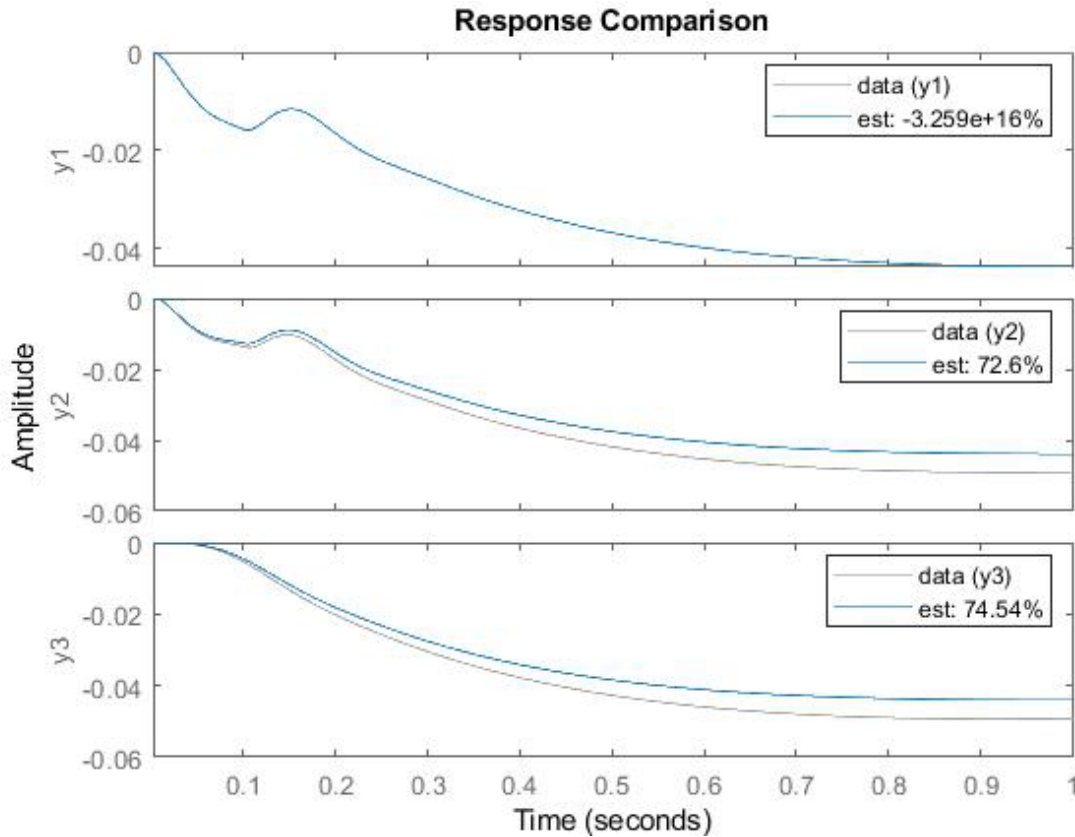


**Figure 35:** Effects of missing data channel on estimation

Note that although the error at mass 1 is very large, the curve looks similar to the one in Figure 32, as the error is calculated between the response from the identified parameters and the response determined by *misdata*, rather than the error between the identified system and the actual system. Still, this missing data results in estimation errors even in the known channels 2 and 3. Figure 36 and Table 23 show the result of the estimation with all these factors. In this example the signal noise was set to an amplitude of 0.1 mm. Changes to the experiment and analysis methodology to mitigate these issues are discussed in more detail in chapter 4.

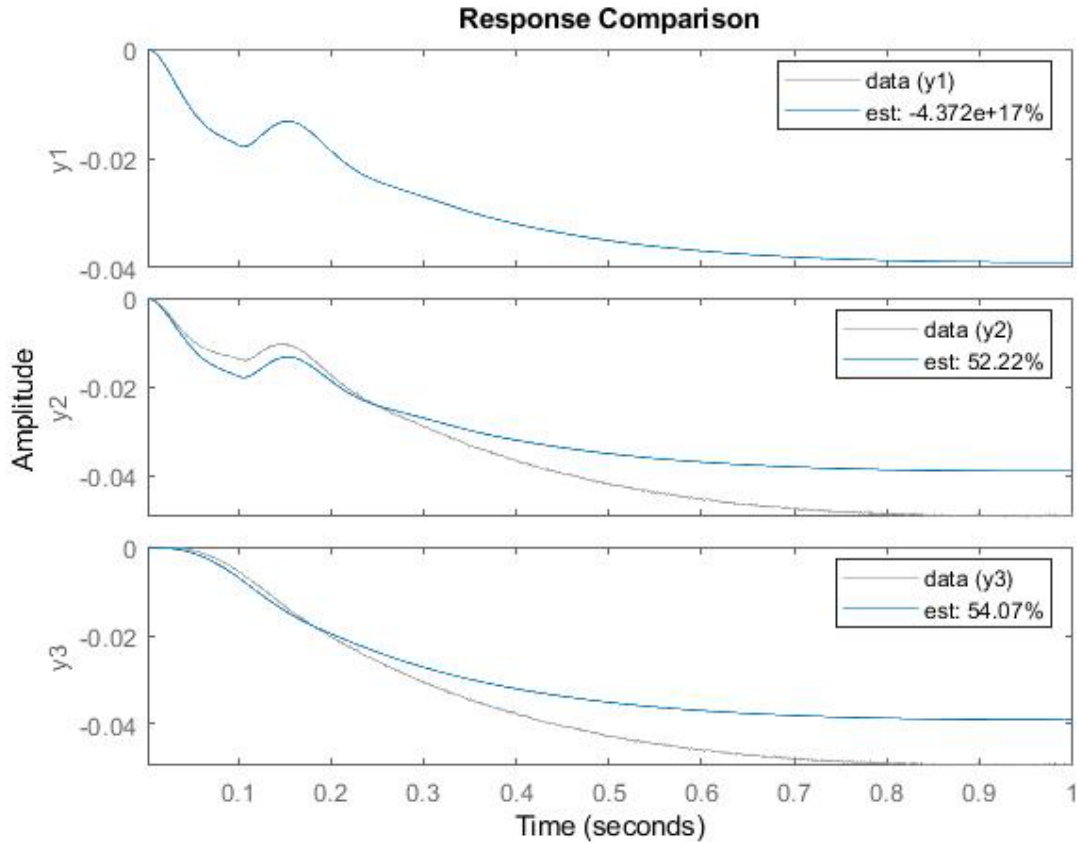


**Figure 36:** Effects of several compounding error sources

**Table 23:** Parameters for estimation with compounding error estimation

Parameter	Initial Value	Estimated Value	Exact Value
$k_1$	654.09	50.62	50
$k_2$	$6.23 \times 10^4$	$2.05 \times 10^7$	$9.41 \times 10^4$
$k_3$	$1.48 \times 10^4$	$9.42 \times 10^3$	$1.01 \times 10^4$
$\alpha$	0.1	4.32	<i>N/A</i>
$\beta$	0.001	3.26	<i>N/A</i>

For the human model presented in the following sections, the effect of these errors will be these reflected in the estimation process. It is clear that the presence of signal noise, a missing data channel, and a proportional damping assumption – in addition to issues with data collection

(sampling rate, number of available sensors etc.) – will contribute to the quality of estimated parameters in the system identification process.

### 3.7 Human Model Structure

The available experimental data corresponds to a human subject stepping on the force plate with one leg with two accelerometers attached to the lower extremity. This is approximated by a 3 degree of freedom model, which is defined by three masses representing three segments of the body as shown in Figure 37(a). At the time of impact, the readings from the force plate are considered as an input excitation and the response are recorded at the accelerometers mounted at mass  $m_1$  and  $m_2$ , as shown in the approximated model in Figure 37(b).

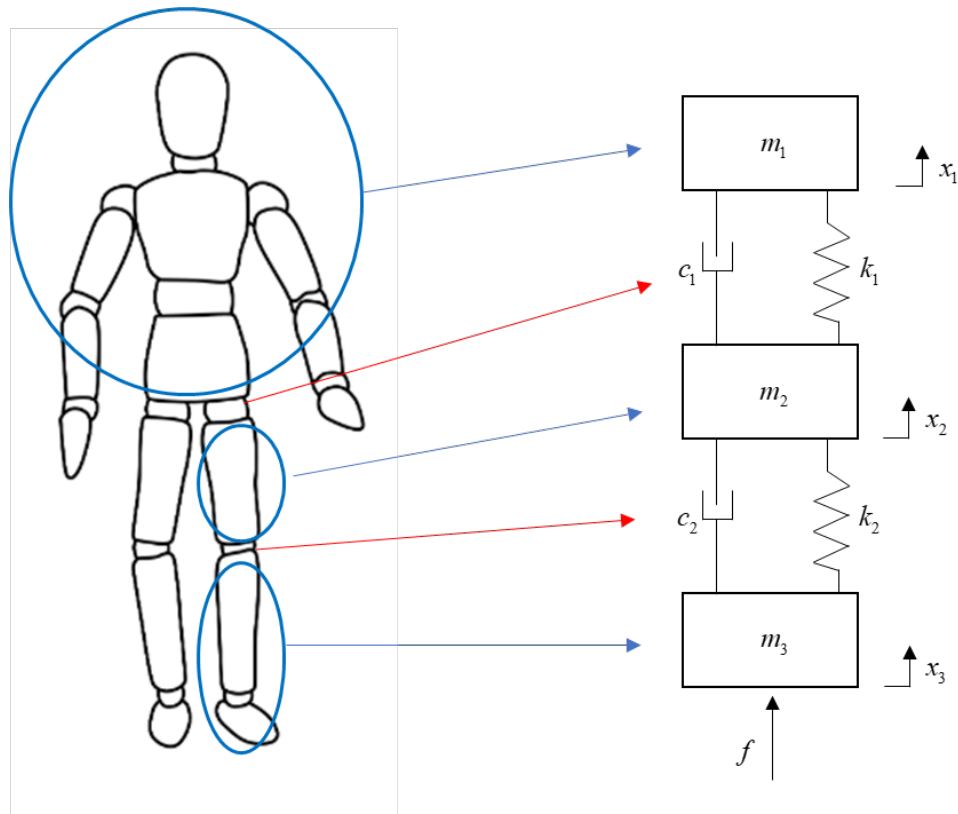


**Figure 37(a):** Human body mass segments

**Figure 37(b):** 3dof vibrational model

Mass values for individual segments can be approximated based on the known weight of each subject and the approximate body mass distribution for an average subject, which is well

studied in the literature, for example in [54]. The relative weights of each body segment are outlined in Table 24 below, which has become the basis for selecting the masses  $m_1$ ,  $m_2$  and  $m_3$  for the system identification process.

**Table 24:** Human body mass distribution

Body Segment	Relative Weight % (male)	Relative Weight % (female)
Whole body	100	100
Trunk	48	50.8
Head and neck	7.1	9.4
Thigh	10.5	8.3
Shank	4.5	5.5
Foot	1.5	1.2
Upper arm	3.3	2.7
Forearm	1.9	1.6
Hand	0.6	0.5

With the approximated mass values, the model shown in Figure 37(b) provides the structure required for a grey-box estimation scheme. It is assumed that the experimental data represent the vibration of the body when excitation force is applied in the vertical axis – that is the axis which is orthogonal to the force plate and parallel to the spine in the standing position. The goal is to estimate the equivalent stiffness and damping parameters ( $k_i, c_i$ ) associated with the bone-muscle system of the lower extremity which satisfies the real physical constraints of these parameters. Note the difference in the excitation assumed in comparison to the previous models. As the subjects are relatively stationary at the moment of contact with the force plate, this system is better approximated as a force-excitation model rather than a base excitation model proposed by Gupta et al [32]. The governing equation for this model is given below. The force plate is zeroed at static equilibrium, where a zero value represents the subject standing with one foot on the plate, therefore the effect of gravity is ignored and the vibration about its static equilibrium position is considered.

$$\underbrace{\begin{bmatrix} m_1 & 0 & 0 \\ 0 & m_2 & 0 \\ 0 & 0 & m_3 \end{bmatrix}}_{\mathbf{M}} \underbrace{\begin{pmatrix} \ddot{x}_1 \\ \ddot{x}_2 \\ \ddot{x}_3 \end{pmatrix}}_{\ddot{\mathbf{x}}} + \underbrace{\left( \alpha \begin{bmatrix} m_1 & 0 & 0 \\ 0 & m_2 & 0 \\ 0 & 0 & m_3 \end{bmatrix} + \beta \begin{bmatrix} k_1 & -k_1 & 0 \\ -k_1 & k_1+k_2 & -k_2 \\ 0 & -k_2 & k_2 \end{bmatrix} \right)}_{\mathbf{C}} \underbrace{\begin{pmatrix} \dot{x}_1 \\ \dot{x}_2 \\ \dot{x}_3 \end{pmatrix}}_{\dot{\mathbf{x}}} + \underbrace{\begin{bmatrix} k_1 & -k_1 & 0 \\ -k_1 & k_1+k_2 & -k_2 \\ 0 & -k_2 & k_2 \end{bmatrix}}_{\mathbf{K}} \underbrace{\begin{pmatrix} x_1 \\ x_2 \\ x_3 \end{pmatrix}}_{\mathbf{x}} = \underbrace{\begin{bmatrix} 0 \\ 0 \\ 1 \end{bmatrix}}_{\mathbf{b}} f(t) \quad (3.18)$$

The proposed model for estimation is shown in Figure 37(c). The leg is represented by two mass elements connects by springs and dampers, which are also connected to an upper-body mass. Consistent with the experiment, an impulse is applied at the lowermost mass corresponding with the ground-reaction force measured by the force plate at the time of the strike. Proportional damping will be assumed for this system, requiring an additional damper element connecting each mass element to a fixed base.

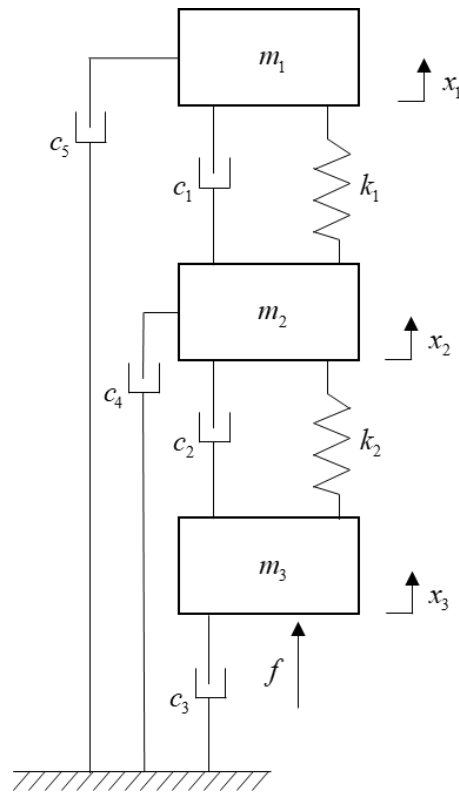


**Figure 37(c):** 3dof vibrational model

While these ground-damper elements may be physically valid representations of the damping provided by the support leg at  $m_1$  and  $m_2$ , the element at  $m_3$  may not be an appropriate representation of the connection between the foot and the base. Nevertheless, it was a necessary compromise and a recognized limitation of this model due to the proportional damping assumption. This can be remedied by the application of additional spring and damper elements, however inconsistencies in the experimental data and errors in the curve fit process make the estimation of more than two spring elements especially difficult. Future studies should seek to improve the quality of subject data and mode pair estimation to allow for estimation of a more valid model. Once the model parameters have been identified, the damping matrix can be resolved by applying the relation,

$$\begin{bmatrix} \beta k_1 + \alpha m_1 & -\beta k_1 & 0 \\ -\beta k_1 & \alpha m_2 + \beta(k_1 + k_2) & -\beta k_2 \\ 0 & -\beta k_2 & \beta k_2 + \alpha m_3 \end{bmatrix} = \begin{bmatrix} c_1 + c_5 & -c_1 & 0 \\ -c_1 & c_1 + c_2 + c_4 & -c_2 \\ 0 & -c_2 & c_2 + c_3 \end{bmatrix} \quad (3.19)$$

Much of the difficulty in identifying model parameters is due to the uniqueness and variability of biological systems. Variations in height and weight mean that the health baseline should vary for different individuals. Body composition also plays a role, as subcutaneous fat should have lower stiffness and higher damping values than skeletal muscle. Refined versions of the model will seek to address these issues.

### 3.8 *Initial System Estimation Algorithm*

In order to find good initial estimates for the parameters of the system, an analytical process for determining some model parameters based on frequency domain information was developed, the steps of which are outlined below.

1. Choose a model a structure and formulate the mass and stiffness matrices.
2. Formulate a state space model of the system with a single force input at the base of the model.
3. Determine mass proportions and values for each element of the mass matrix using approximate biological mass distribution.

4. Use the natural frequencies and their associated damping ratios  $(\omega_i, \zeta_i)$  obtained from the modal analysis process described in chapter 2 for each individual as an input in this model.
5. Determine the constants  $\alpha$  and  $\beta$  of the proportional damping matrix,

$$\mathbf{C} = \alpha\mathbf{M} + \beta\mathbf{K} \quad (3.20)$$

from the knowledge of  $(\omega_i, \zeta_i)$

$$\zeta_i = \frac{\alpha}{2\omega_i} + \frac{\beta\omega_i}{2}, \text{ for } i=1,2,\dots, \quad (3.21)$$

in a least squares sense.

6. Determine the stiffness parameters  $k_1, k_2, \dots$  from the definitions of the resulting eigenvalue problem,

$$\det(\mathbf{K} - \omega_i^2\mathbf{M}) = 0 \quad (3.22)$$

7. Simulate the response of this model when excited by the ground reaction force measured at the force plate.
8. Compare the simulated response to the experimental response and quantify by determining the mean relative error between the two signals.
9. Iteratively improve the model by selecting different frequency/damping pairs, tweaking mass proportions, or increasing model order.

Errors between the simulated model and the experimental response are expected for several reasons. The process used to determine the frequency damping pairs relies on an inexact curve fit, so the pairs used may either be imperfect or entirely irrelevant. While the acceleration data represents the axial motion of each accelerometer, this motion is not always due to axial vibration of the model. The model is constrained such that it only moves in the vertical direction, while a human subject moves in three dimensions. Bending/swaying modes will result in axial motion of the sensors, so some frequency-damping pairs may be invalid for the axial model. Additionally, there is test-to-test variation in the experimental data resulting from subject behavior and other external factors, and this model does not take into account the relative motion between the skin-mounted sensors and the subject mass elements. Finally, this model approximates a human subject, an actively controlled system, as a passive system.

### 3.9 Application of Analytical Estimation

For acceleration outputs for system of this structure, the output matrix  $\mathbf{C}_{state}$  is as follows which returns the acceleration of the system at each at each degree of freedom,

$$\mathbf{C}_{state} = \begin{bmatrix} \frac{-k_1}{m_1} & \frac{k_1}{m_1} & 0 & \frac{-(\beta k_1 + \alpha m_1)}{m_1} & \frac{\beta k_1}{m_1} & 0 \\ \frac{k_1}{m_2} & \frac{-(k_1 + k_2)}{m_2} & \frac{k_2}{m_2} & \frac{\beta k_1}{m_2} & \frac{-(\alpha m_2 + \beta(k_1 + k_2))}{m_1} & \frac{\beta k_2}{m_2} \\ 0 & \frac{k_2}{m_3} & \frac{-k_2}{m_3} & 0 & \frac{-\beta k_2}{m_3} & \frac{(\beta k_2 + \alpha m_3)}{m_3} \end{bmatrix}, \quad (3.23)$$

while the feed-forward matrix is assumed to be zero implying  $\mathbf{D} = \mathbf{0}$ .

A single subject file (“subject 1”) was selected for the system identification, in order to estimate its stiffness and damping parameters. The mass of this subject is 69.8 kg. The distribution of subject mass values is shown in Table 25 below, and was calculated using the geometric properties proposed by Tözeren [54]. The uppermost mass is assumed to be the difference of the total mass and the mass elements of the leg and foot.

**Table 25:** Estimated mass distribution for subject 1

Element	Mass Proportion	Mass Value
Foot + Shank, ( $m_3$ )	6.7 %	4.67 kg
Thigh, ( $m_2$ )	8.3 %	5.79 kg
Upper Body, ( $m_1$ )	85 %	59.33 kg

By following the vibration data analysis process described in chapter 2, the time domain data associated with subject 1, shown in Figure 38, was converted into the frequency domain.

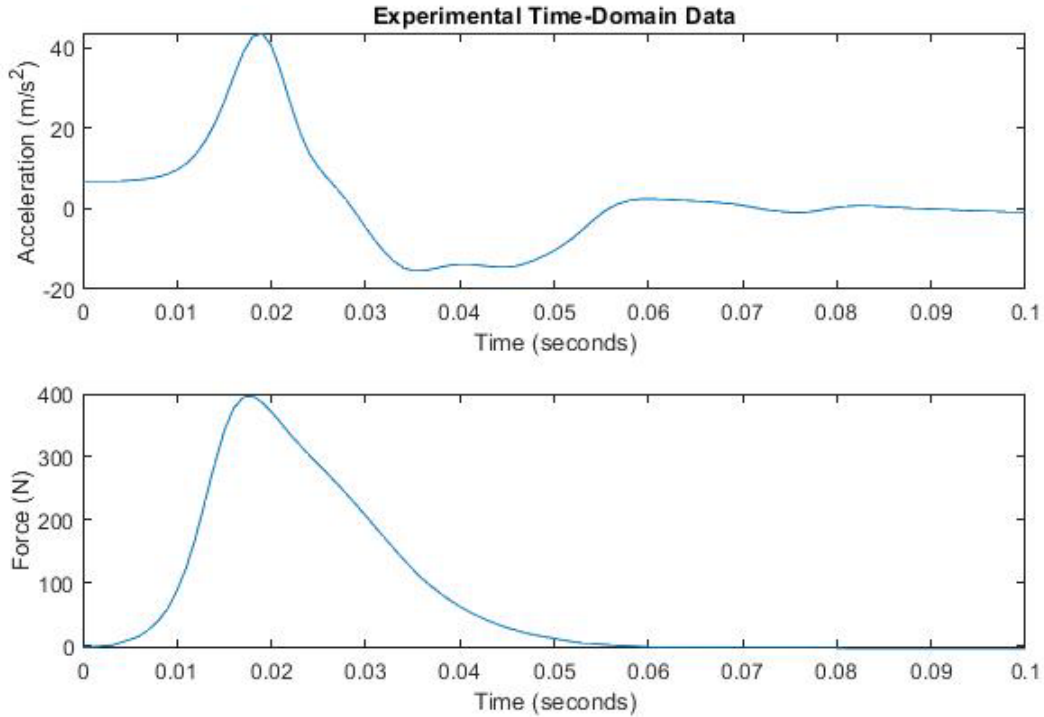


**Figure 38:** Time domain data for one mass and a single test

A modal stabilization diagram was then generated to provide an initial estimate for the order of a curve fit to determine the natural frequencies and damping ratios. For the three degree-of-freedom model, only the low to middle frequencies are considered, so this analysis was constrained to frequencies below 140 Hz. The stabilization diagram for the frequency response transfer function of subject 1 is shown in Figure 39. Frequency domain curve-fitting is carried out as described in chapter 2 resulting in 3-4 identifiable peaks in the region of interest. Note the smoothness of this curve relative to the one presented in Figure 13. Estimation in this lower frequency range is especially susceptible to estimation errors. Minor changes to the curve order or frequency boundaries can have major effects on the estimated frequency-damping pairs in this region. From this fit, four natural frequencies were identified, shown in Table 26.

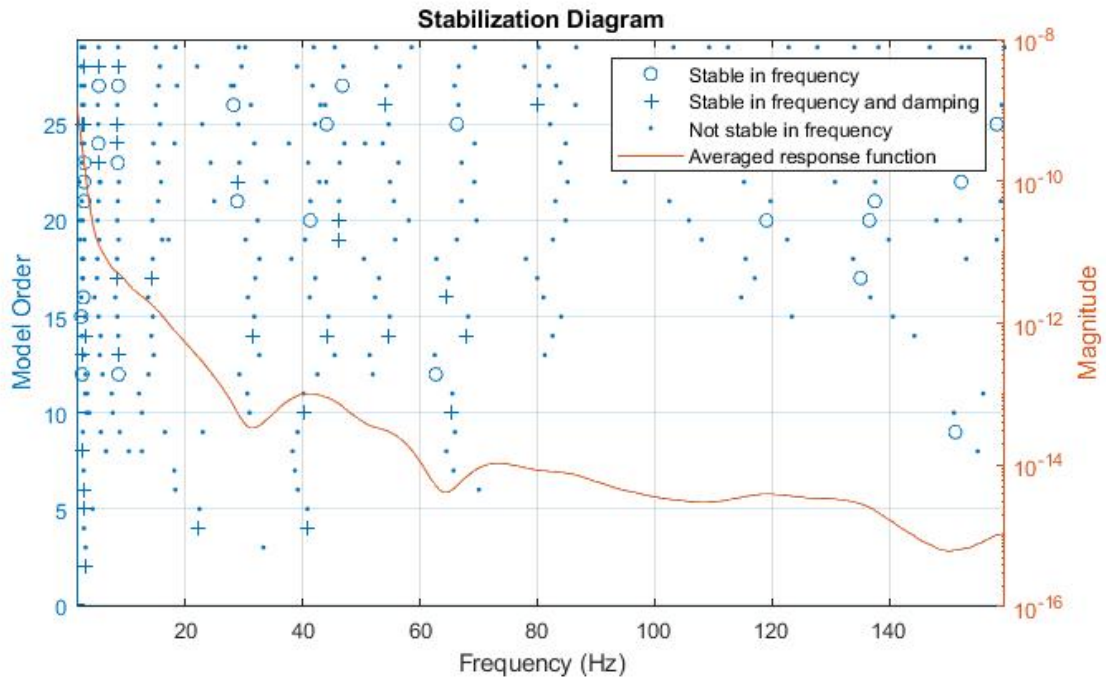


**Figure 39:** Example of modal stabilization diagram used to estimate curve order

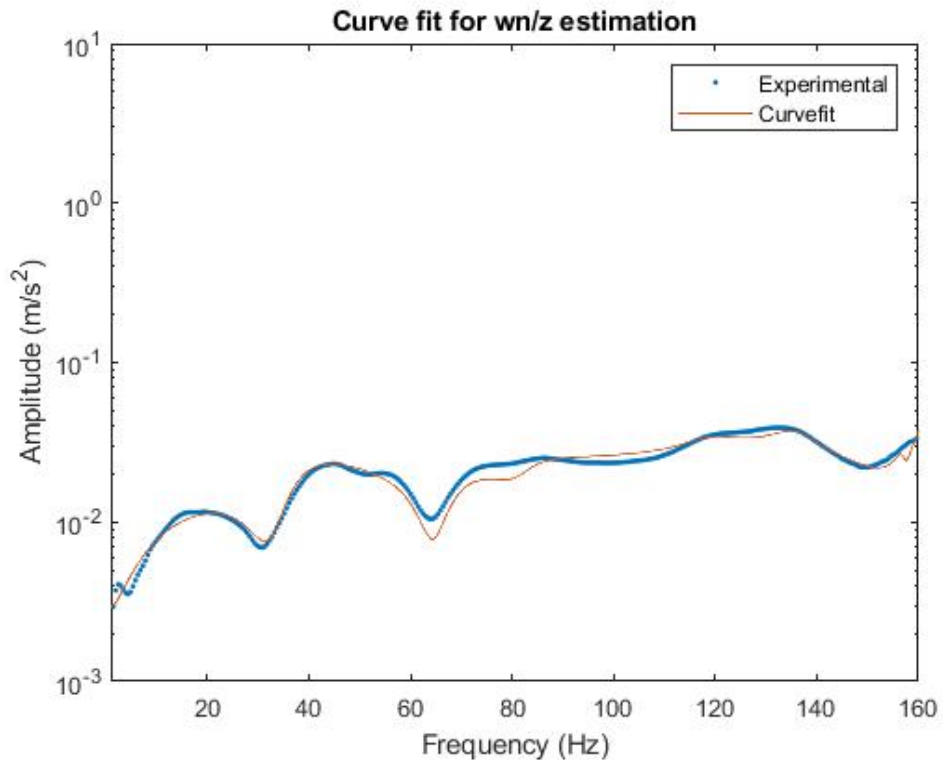


**Figure 40:** Example of fitted curve for mode pair identification

**Table 26:** First four frequency damping pair for subject 1

Index	Frequency (Hz)	Damping Ratio
1	36.85	0.1947
2	66.27	0.1096
3	82.37	0.069
4	118.87	0.0574

By fixing the mass values, and hence mass matrix  $\mathbf{M}$ , from Table 22, two frequency/damping pairs were needed for the identification algorithm to determine values for unknown stiffness and damping constants. Through trial and error, two frequencies from Table 23 were selected such that the real solutions for the initial estimates of stiffness parameters and corresponding stiffness matrix  $\mathbf{K}$  can be computed from (3.22). Subsequently, by using the corresponding damping ratio, proportionality constants  $\alpha$  and  $\beta$  are calculated from (3.21). These initial estimates are tabulated in Table 27, below.

**Table 27:** Initial estimates of stiffness and damping parameters for subject 1

Parameter	Value
$k_1$	$2.66 \times 10^6$ N/m
$k_2$	$2.50 \times 10^5$ N/m
$\alpha$	90.63
$\beta$	-0.0000087

With the knowledge of these parameters the damping matrix  $\mathbf{C}$  is obtained from (3.20). The initial estimates of system matrices are used to compute the acceleration output from (3.23) by solving the state space system (3.14) due to force excitation input shown in Figure 38. These acceleration response is compared with the experimental response of subject 1 in Figure 41. The sum of squared residuals known as error norm at position 1 and position 2 were calculated to be 2239 and 4459 respectively.

In order to improve the estimation, the initial estimates of mass proportions were changed. Mass 1 was redefined such that it does not include the mass of the stationary leg. This assumption resulted in a reduction of upper body mass from 85% of total mass to 70% of the total mass. Hence the modified values of masses are obtained to be 48.65 kg, 5.77 kg, and 4.66 kg respectively. The simulated acceleration response with these mass values and the values from Table 24 are compared with the experimental acceleration response in Figure 42. It can be seen that a better estimation is realized and the resulting error norm at position 2 is the same as previous case, however error norm at position 1 was decreased to 1942.

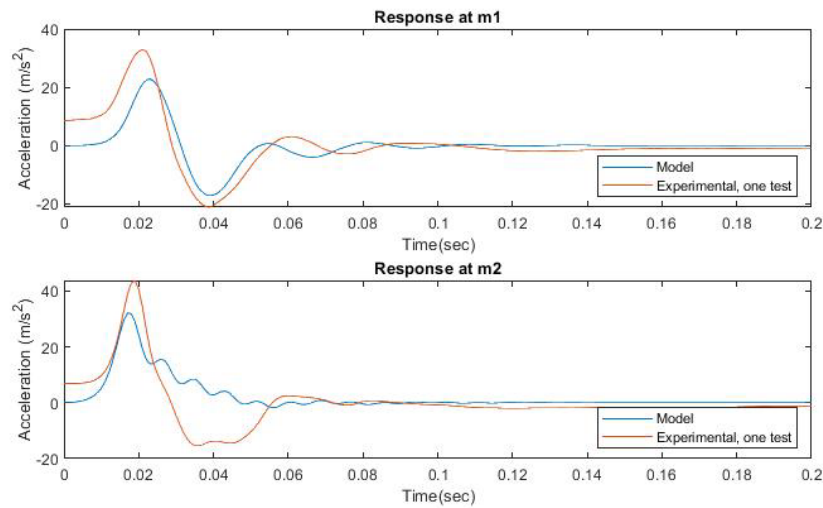


**Figure 41:** Comparison of simulated and experimental responses

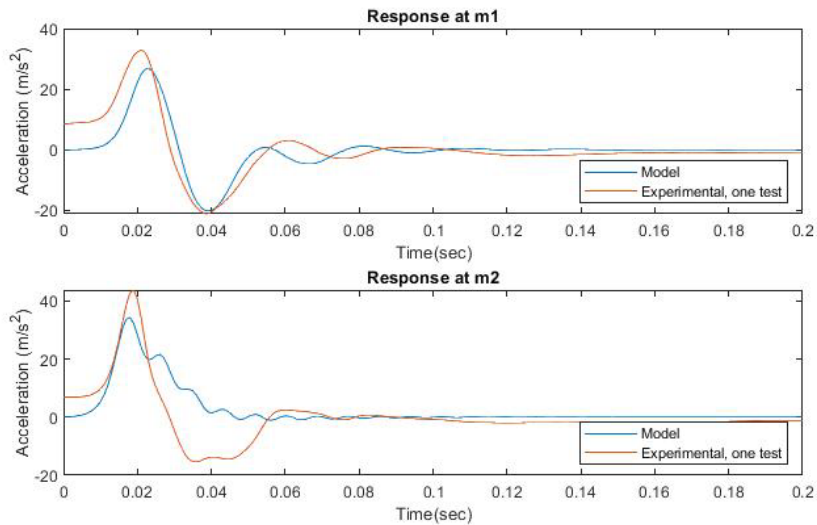


**Figure 42:** Comparison of responses with modified mass distribution

It is important to note the difference in initial acceleration between the model and the experimental results. Majority of difference is originated from the mismatch in the initial value of the acceleration. The acceleration response from the estimated model is computed with the assumption of zero initial condition on the state variables (initial displacement and initial velocity), which were not available, therefore accurate initial conditions may be needed for response estimation. The experimental data suggests that the experiment was set to begin recording when the force plate reached the trigger value of 10 newtons, and only five samples before this trigger were taken resulting the initial force and acceleration values to be non-zero. Hence, in order to the initial conditions of the system, a piecewise spline curve fit was applied to each signal, as shown in Figure 43.

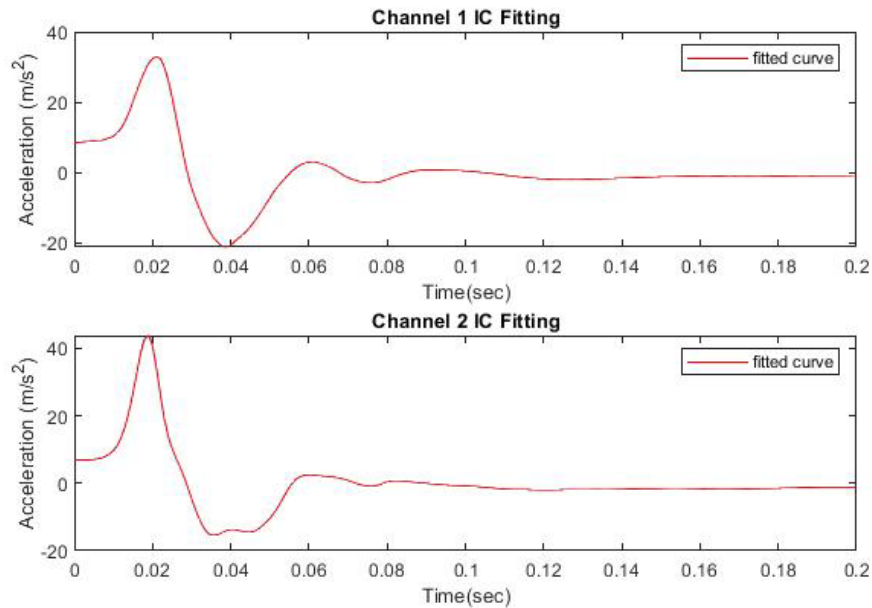


**Figure 43:** Fitted curves for determination of initial conditions

The equation for each fitted curve was then integrated twice to determine an estimate for the initial velocity and displacement conditions. Estimates of these initial conditions are tabulated in Table 25.

**Table 28:** Estimated initial conditions from curve fit

	Channel 1	Channel 2
Initial Velocity	$5.52 \times 10^{-4}$ m/s	$4.80 \times 10^{-4}$ m/s
Initial Displacement	$2.76 \times 10^{-10}$ m	$2.40 \times 10^{-10}$ m

These initial conditions were then applied to the state space model along with the initial estimates of system matrices, which resulted in a significant decrease in model quality. This model is a three degree-of-freedom system, but only two sensors are available for analysis, therefore the initial conditions for the third element cannot be readily estimated by fitting the numeric data. Manual, iterative estimation of the initial conditions was then attempted. Both channels improved just slightly, particularly in the region near  $t=0$ , with the sum of squared error becoming 1524 and 4559 for channels 1 and 2, respectively. This final estimation is shown in Figure 44. To overcome these challenges, during the system identification process described in the following section, the option *InitialState* can be set to *auto* to allow MATLAB to automatically determine the best conditions for the initial states.

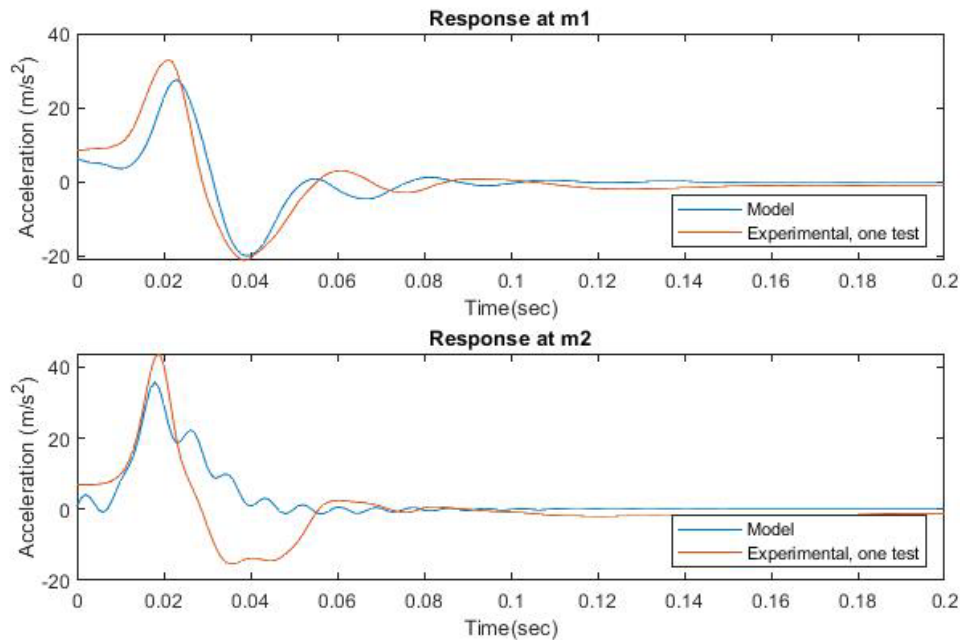


**Figure 44:** Comparison of responses with initial velocity condition

### 3.10 *Parameter Estimation using Experimental Data and System Identification Toolbox*

By following the procedure in Section 3.6, the system identification toolbox is used for the experimental setup described in Chapter 2. For this experimental setup, there is no sensor at  $m_3$ , which requires the missing data to be reconstructed. The *misdata* command was applied here to estimate the missing channel using the state space model obtained analytically. While the initial estimates of model parameters identified in section 3.8 is imperfect, it is suitable for this system identification algorithm and it serve as initial conditions. However, estimation of the missing channel results in a singularity at the first time value, was remedied by removal prior to system identification.

The time-domain experimental data, the input force data and state responses, is passed to *greyest* function that implements the system identification process using the model defined by *idgrey*. In the first example, the masses and damping constants are kept as fixed values of initial estimates (from section 3.7) and unknown stiffness parameters are identified using this process. The identified values with initial estimates are show in Table 29 and the estimated response is compared with the actual experimental response in Figure 45. This estimation shows minimal change in the stiffness from the initial estimates, around 5-10% for each stiffness values. The percentage in Figure 45 quantifies the estimate quality by the normalized root-mean-square error.

**Table 29:** System parameters with estimable stiffness

Parameter	Initial	Estimated
$m_1$	48.86	48.86
$m_2$	5.79	5.79
$m_3$	4.67	4.67
$k_1$	$2.66 \times 10^6$	$2.09 \times 10^6$
$k_2$	$2.50 \times 10^5$	$2.56 \times 10^5$
$\alpha$	90.63	90.63
$\beta$	-0.0000087	-0.0000087

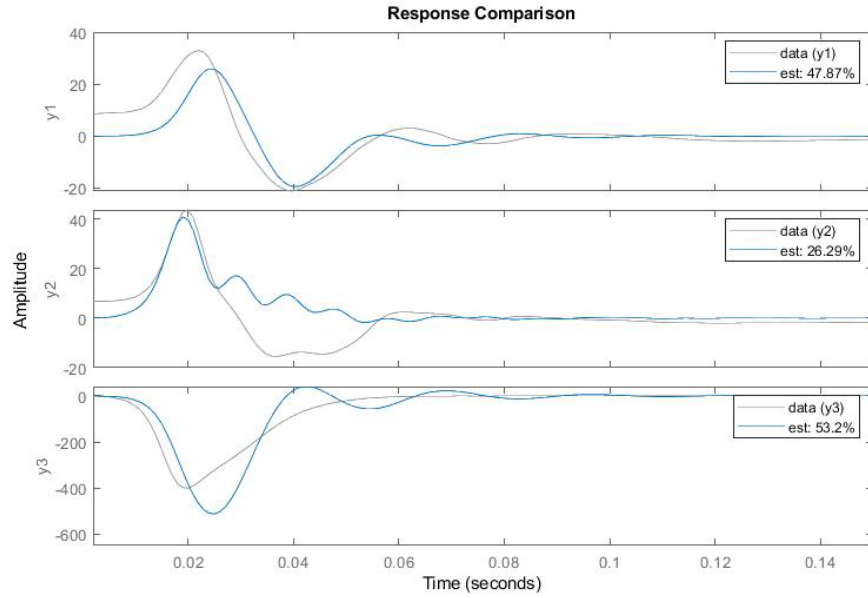


**Figure 45:** Identified system with estimable stiffness

To verify that the identified model is an improvement over the initial system, both responses are plotted along with the raw experimental data in Figure 46, comparing this estimation to the initial system shown in Figure 42. Note the slight change in peak amplitude for the identified system.

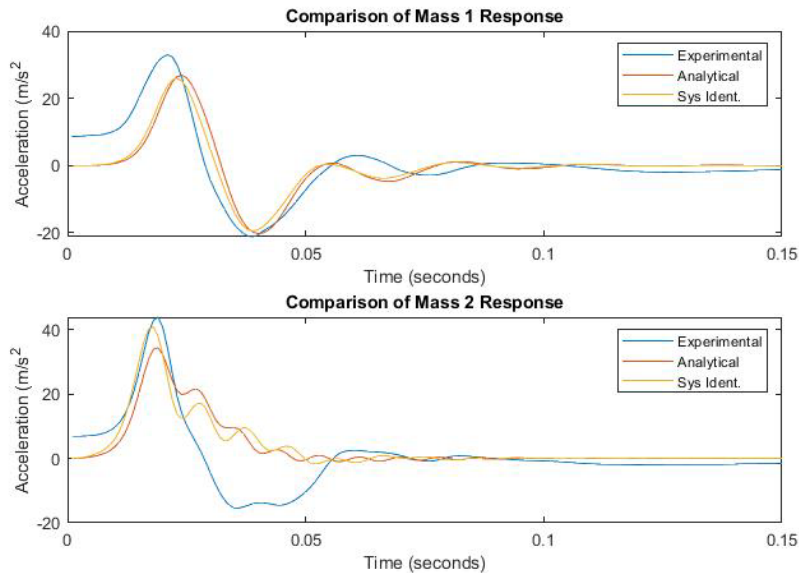


**Figure 46:** Comparison of experimental data, initial system, and identified system for verification

Next the estimation is improved upon by assuming both the damping constants and the stiffness values to be free parameters. The estimated parameters for this case is shown in Table 27 and the estimated responses are compared with the experimental one in Figure 47. It is evident from Figure 47 that the estimation improves by about 10% at position 2, while the estimation at position 1 remains roughly the same. A 10% improvement is also shown in the fit for the reconstructed channel at position 3.

**Table 30:** System parameters with estimable stiffness and damping

Parameter	Initial	Estimated
$m_1$	48.86	48.86
$m_2$	5.79	5.79
$m_3$	4.67	4.67
$k_1$	$2.66 \times 10^6$	$2.66 \times 10^6$
$k_2$	$2.50 \times 10^5$	$2.82 \times 10^5$
$\alpha$	90.63	128.05
$\beta$	-0.0000087	0.00022

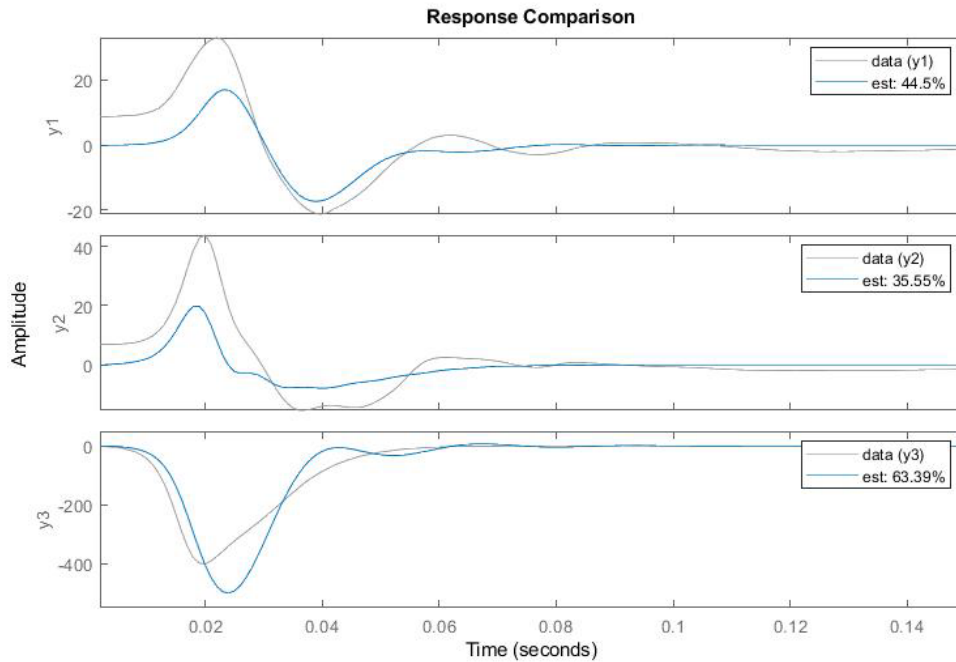


**Figure 47:** Identified system with estimable stiffness and damping

Finally, for the system identification all the parameters (mass, stiffness and damping constants) are assumed to be free variables. The initial mass values are imperfect estimates, depending not only on the assumption that the proportions are roughly equal for all humans, but also on the assumption that each mass element is discrete. In reality the mass distribution of the human leg is continuous, and the relatively close proximity of the tibial tuberosity and lateral femoral condyle accelerometers further negates the accuracy of the initial mass approximations. This model also fails to account for the support provided by the stationary leg, so the estimated mass of the upper body should be lower than the actual mass.

The model was then identified by freeing and unbounding the mass parameters. The estimation is significantly improved for all degrees of freedom as shown in Figure 48 for the case of free mass values however the estimated mass values do not make physical sense, as shown in Table 28. This was refined once more, by bounding the mass parameters to within  $\pm 20\%$  of their initial values, the result of which is shown in Figure 49 and the estimated parameters are shown in Table 28. Curiously, this resulted in a decrease in estimation quality that of the fixed mass value. This was remedied by fixing the damping constants, but overall does not seem to be a viable criterion for identification. A comparison of these two estimation schemes is shown below in Table 31.

**Table 31:** System parameters with estimable mass, stiffness, and damping

Parameter	Initial	Unbounded Mass	Bounded Mass
$m_1$	48.86	8.74	53.74
$m_2$	5.79	0.10	6.37
$m_3$	4.67	36.67	4.90
$k_1$	$2.66 \times 10^6$	$2.57 \times 10^6$	$2.66 \times 10^6$
$k_2$	$2.50 \times 10^5$	$7.98 \times 10^5$	$2.74 \times 10^5$
$\alpha$	90.63	601.67	90.63
$\beta$	-0.0000087	0.0000018	-0.0000087

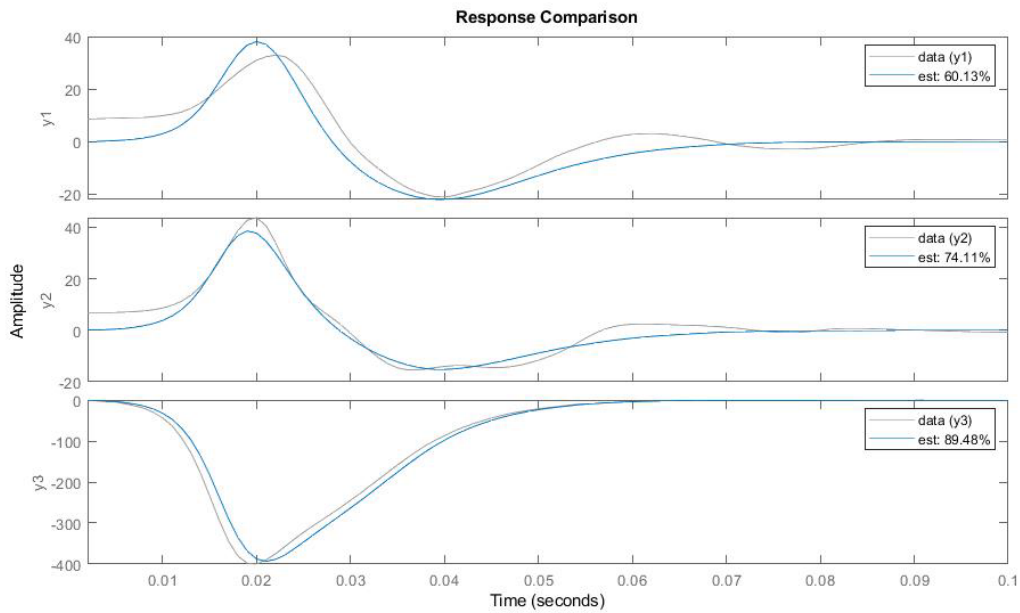


**Figure 48:** Identified acceleration response with free mass, stiffness, and damping

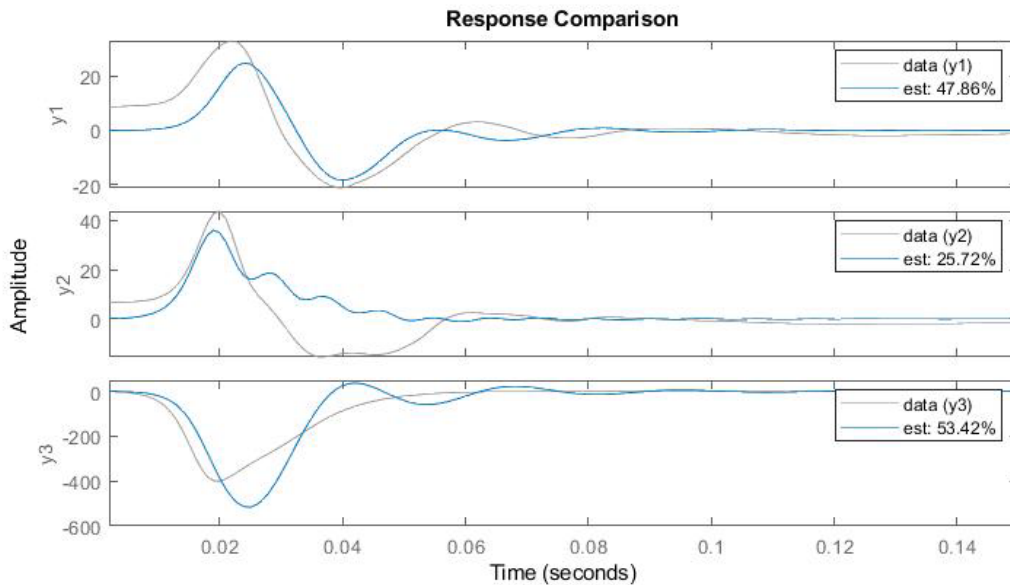


**Figure 49:** Identified acceleration response with bounded mass, free stiffness and damping

Of the four constraint setups above, the fixed mass/estimable stiffness and damping produced the best results without providing unrealistic estimates for the mass. From here, the

damping values can be calculated for the model assumed for subject 1 in Figure 37(c), and the final model assembled by applying equation (3.19).

**Table 32:** Estimated values for model elements

Parameter	Estimated Value
$m_1$	48.86 kg
$m_2$	5.79 kg
$m_3$	4.67 kg
$k_1$	$2.66 \times 10^6$ N/m
$k_2$	$2.82 \times 10^5$ N/m
$c_1$	$0.585 \times 10^3$ Ns/m
$c_2$	$0.062 \times 10^3$ Ns/m
$c_3$	$0.598 \times 10^3$ Ns/m
$c_4$	$1.326 \times 10^3$ Ns/m
$c_5$	$6.565 \times 10^3$ Ns/m

The quality of the estimates for each channel are expressed in the comparative outputs and are 44.5%, 35.5%, and 63.9% for positions 1, 2, and 3, respectively. These values are consistent with those demonstrated in section 3.6, and are the likely results of issues similar to those described in that section: signal noise, a missing data channel, and the proportional damping assumption, in addition to the possible issues in the experiment setup (sampling rate, number of available sensors etc.) described in chapter 4. Future studies should seek to improve the estimates by mitigating these factors.

### 3.11 *Effects of Body Mass Index on Identified Parameters*

To further investigate how a subject's physical composition affects the results, a comparative analysis of four subjects in the same group but with varying body-mass index (BMI) was performed. It was hypothesized that an increase in subject mass will result in an increase in estimated stiffness, as an increase in subject mass corresponds to an annular increase in soft tissue

around the bones. Three additional subjects with different BMI were selected at random for comparison and identified by the same process described in previous sections. Consistent with subject 1, the first and fourth estimated modes shown in Table 33 were chosen for the identification process.

**Table 33:** Identified modes for three subjects with varying mass

Parameter	Subject 1	Subject 2	Subject 3	Subject 4
frequency 1	36.85	38.10	35.34	37.47
frequency 2	118.87	132.03	104.62	138.77
damping 1	0.1947	0.4056	0.289	0.1917
damping 2	0.0574	0.0511	0.108	0.1295

By the process described in sections 3.8 and 3.9, an initial system was identified analytically, the missing data channel was approximated, and grey-box identification was performed to obtain the final values. For the system identification process, mass was left as a fixed parameter while stiffness and damping were kept as free parameters. For subject 2, the damping constant had to be fixed at the initial value to obtain a high-quality estimate. The final estimated properties for each subject are outlined in Table 34.

**Table 34:** Comparative analysis of subjects with varying mass

Parameter	Subject 1	Subject 2	Subject 3	Subject 4
BMI	27.1	30.0	34.3	50.7
$k_1$	$2.66 \times 10^6$	$3.84 \times 10^6$	$3.62 \times 10^6$	$4.89 \times 10^6$
$k_2$	$2.82 \times 10^5$	$1.76e \times 10^5$	$2.37 \times 10^5$	$5.58 \times 10^5$
$\alpha$	128.05	204.16	138.21	114.67

These preliminary findings indicate a possible correlation between increased subject mass and increased structural stiffness at the first stiffness element, which is consistent with the hypotheses, however the trend for the second element is less clear, as demonstrated in Figure 50.

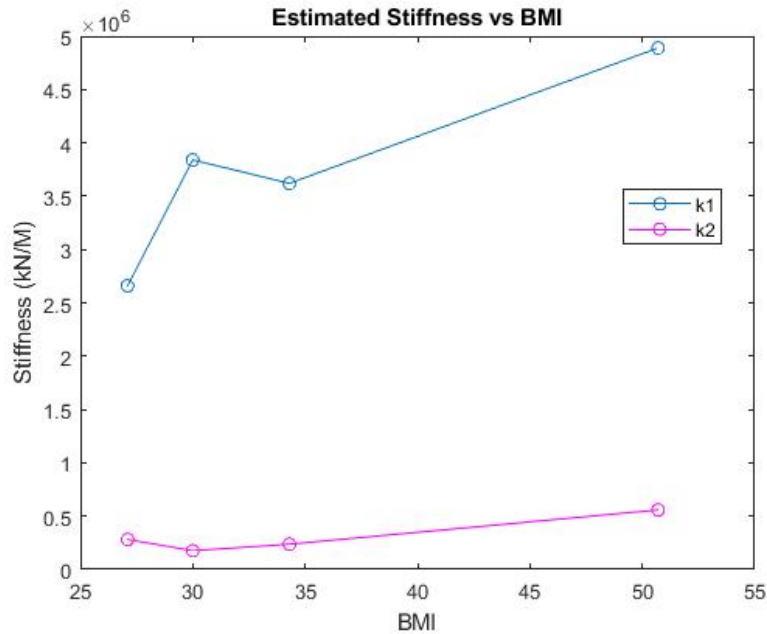


**Figure 50:** Estimated stiffness plotted against subject BMI

Initial stiffness values are heavily dependent on the estimated modes, which can be unclear in the lower frequency regions, so to confirm these findings, rigorous identification and statistical analysis of all subjects is required in the future. As the effects of bone quality on the identified system are likely significantly smaller than those of individual subject mass composition. While it was possible to compare effects of body mass by taking several subjects from the same group to control for lead-levels, the sample does not provide subjects with identical body-mass index values in each group, therefore preliminary analysis of this factor by comparison of individual subjects is not possible.

## 4. Conclusion

In this research vibration characteristics (natural frequencies and damping ratio) of human subjects exposed to various lead exposure levels were investigated and the damping properties of their lower extremities were correlated with lead levels. These vibration parameters and experimental data are also used for estimating the parameters needed to construct a mathematical model corresponding to the lower extremity of a given subject. The vibration analysis technique and system (model) identification process developed in this research may become the basis for continuous monitoring of the dynamic bone health and may serve as early indicators for Osteoporosis and other bone/muscle related diseases. The summary of the results from this study are summarized here and some potential ideas to improve the system identification is discussed in the subsequent sections.

### 4.1 *Summary of results*

The research can be classified into two distinct phases. Phase one dealt with the vibration analysis of clinical data provided by University of Cincinnati (UC) and in the second phase vibration characteristics and available experimental data were utilized in reconstructing mathematical model for a given subject based on the system identification technique.

During the first phase of this research, vibration analysis of clinical data for 179 patients (subjects) provided by UC researchers were carried out. The analysis was targeted to (i) extract modal parameters (natural frequency and damping ratio) from the clinical data, (ii) estimate the changes in structural damping corresponding to higher modes in patients, and, (iii) find the potential correlation with bone density and increased fracture risk corresponding to different lead exposure level in the subjects. Vibration-based diagnostic tools are used to extract the modal parameters (natural frequencies, damping, modes etc.) and subsequently statistical analysis is carried out. To that end, the following tasks have been accomplished:

- Frequency response transfer functions have been extracted from approximately 3,580 time-domain test data corresponding to multiple tests on 179 clinical subjects.

- Frequency and damping pairs have been estimated from these frequency response functions (FRFs) for a frequency range of 0-500 Hz.
- Dominant modes are identified by classifying high density regions for each group as well as overall subject population.
- Statistical clustering tools are developed and employed to identify bin boundaries corresponding to dominant modes, such that damping properties around these modes are identified and used for correlation with lead levels in patients.
- Mean damping values for overall population and subject groups have been determined and ANOVA analysis is carried out indicating a correlation between the estimated damping ratios and blood-lead concentration.

The second phase focused on the system identification and validation of the model based on available clinical data. The following tasks were completed:

- For system identification, various tools are investigated, and a linear state space system model is selected for the identification process.
- Initial estimates of the model parameters (mass, stiffness, and damping constants) were obtained analytically for individual subject based on frequency-damping pairs identified using the process developed in phase one.
- Various assumptions on the frequency-damping pairs were tested and compared for estimating the parameters analytically.
- Using the analytical three degree of freedom human model, the missing data from the 3<sup>rd</sup> degree of freedom was estimated to be used for subsequent system identification process.
- A grey-box system identification model was developed consistent with the three degree of freedom human model used for analytical identification.
- System identification was performed using the grey-box estimation algorithms using the MATLAB System Identification Toolbox. Three different constraint scenarios were investigated and compared to improve the quality of the estimation.

- The quality of the estimated parameters was quantified by comparison to the experimental data.
- A preliminary comparative analysis of stiffness values with respect to variation in subject mass distribution or BMI was carried out.

The accuracy of identified model project was limited by the experimental setup used to generate the subject data, as it was performed for extracting vibration parameters and not for system identification process. Some changes to the experimental setup are proposed in the next section, which will allow the developed process for a more accurate system identification.

## 4.2 *Discussion*

There are several factors influencing the quality of estimations for the proposed human model, some of which are explored in section 3.6. The placement of the damping elements in the model results in positive values for each, however this model and estimation strategy could be improved by direct estimation of the damping elements, which would allow for construction of a model that is not dependent on the proportional damping assumption. This would allow the damping elements ( $c_3$ ,  $c_4$ ,  $c_5$ ) necessary to satisfy equation (3.19) to be moved or removed as necessary. High quality initial estimates are required these values, which may be determined by iteratively testing different combinations of damping parameters. While this compromise was necessary to identify the model based on the provided data, improved experimental data may make it more feasible to directly estimate the damping elements.

The experiment performed to generate the subject data used in model identification was designed to correlate bone-lead contamination with changes in the damping ratios measured at the first natural frequency. To improve the model development, several changes may be made to the experimental setup. The force trigger value was likely set too high and recorded too few pre-trigger samples, making the initial state of the system difficult to resolve. Few accelerometers were used, and the lowermost sensor was positioned just below the knee, which failed to capture system dynamics at the ankle and foot. The accelerometers only captured acceleration in the

vertical direction, making it impossible to determine whether the curve fit process is capturing solely axial modes, or vertical displacement due to transverse motion at shown in Figure 51 below. This could be remedied by using tri-axial accelerometers to identify and neglect transverse modes, or by constraining subject motion to the vertical direction using braces or tracks.

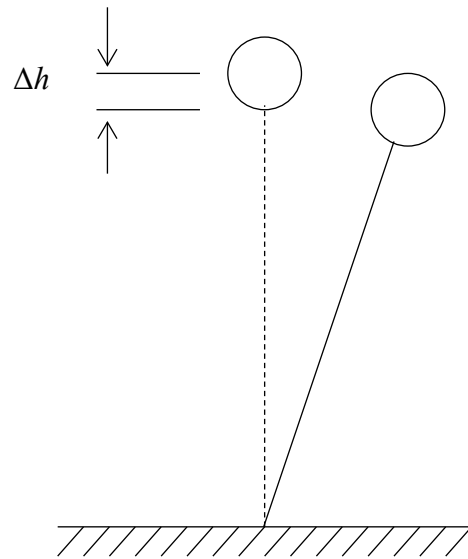


**Figure 51:** Vertical displacement due to transverse flexural motion

Additionally, the positioning of the lower accelerometer just below the knee requires that the lower portion of the system be approximated by a single stiffness and damping value. In reality there are several elements in this system with different values: the shoe, the foot, the ankle, the shank, and the parallel stiffness and damping provided by the tissue surrounding the bone. An experiment designed for the express purpose of developing a mathematical model of the structure would benefit from tri-axial accelerometers placed at the union of each of these elements in addition to those used in the current experiment as show in Figure 52. As the primary contributor to estimation errors in this study was the missing data channel at the lowermost mass, the addition of at least one accelerometer should dramatically increase the estimation quality.

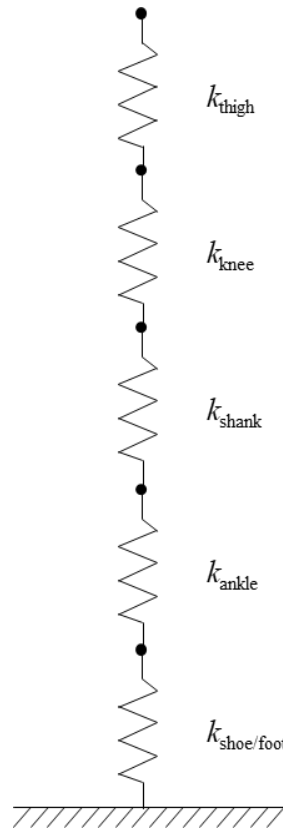


**Figure 52:** Placement of additional accelerometers

The mass and attachment method of the accelerometers may also obfuscate the results. Past studies demonstrated that skin mounted accelerometers may be insufficient in capturing bone acceleration and may instead be capturing the vibration of soft tissue between the bone and the sensor. This study was limited to frequencies below 500 Hz, while the dominant axial vibrational mode of the skeletal bone in the leg occurs around, at a minimum, 2000 Hz [28–30]. To remedy this, a higher frequency range should be measured and accelerometers should either be placed in direct contact with the bone using the method demonstrated by Ziegert and Lewis, or secured tightly with straps rather than mounted loosely with double-sided tape.

Despite the issues in capturing bone mechanics using the relatively low-frequency measurements, it was demonstrated that decreases in damping ratios at these frequencies do in fact correlate to decreases in bone quality. These two conclusions seem to disagree, however there is a biological explanation. As flexural vibration modes were demonstrated at as low as 200 Hz, and the experimental data does not provide a way to distinguish between axial and flexural vibration,

it is possible that at least one of the identified prominent modes occurs in the transverse plane. However, a more likely theory involves the interconnectedness of bone degeneration and soft-tissue changes. Osteoporosis is a complication of aging, and is interconnected with sarcopenia, or decreasing muscle mass, and adiposity, or increasing fat mass. Sarcopenia affects a person's ability to regulate balance and may have affect the damping ratios measured at natural frequencies associated with postural sway. Additionally, the loss of muscle mass in conjunction with the increase in fat mass in the tissue layers between the accelerometer and the bone may result in lower damping ratios. This may be exacerbated by the fact that the test subjects were not only osteoporotic or pre-osteoporotic, but were also exposed to unsafe concentrations of blood lead, which has been known for decades to have a deteriorating effect on many tissues of the body.

This research study highlights that with systematic design of clinical studies, a non-invasive tool for monitoring the dynamic health of bone/muscles can be developed which can aid in developing future diagnosis technologies for various diseases.

## 5. References

- [1] Ettinger, B., Black, D. M., Dawson-Hughes, B., Pressman, A. R., and Melton, L. J., 2010, “Updated Fracture Incidence Rates for the US Version of FRAX®,” *Osteoporos. Int.*, **21**(1), pp. 25–33.
- [2] National Osteoporosis Foundation, 2015, “Osteoporosis Fast Facts” [Online]. Available: <https://cdn.nof.org/wp-content/uploads/2015/12/Osteoporosis-Fast-Facts.pdf>.
- [3] Seeley, D. G., Browner, W. S., Nevitt, M. C., Genant, H. K., Scott, J. C., and Cummings, S. R., 1991, “Which Fractures Are Associated with Low Appendicular Bone Mass in Elderly Women?,” *Ann. Intern. Med.*, **115**(11), pp. 837–842.
- [4] Gullberg, B., Johnell, O., and Kanis, J. A., 1997, “World-Wide Projections for Hip Fracture,” *Osteoporos Int*, **44**(1997), pp. 407–413.
- [5] American Bone Health, 2009, “How Often Should I Get Tested?” [Online]. Available: <https://americanbonehealth.org/bone-density/how-often-should-i-have-a-bone-density-test/>.
- [6] Liu, X. S., Sajda, P., Saha, P. K., Wehrli, F. W., and Guo, X. E., 2006, “Quantification of the Roles of Trabecular Microarchitecture and Trabecular Type in Determining the Elastic Modulus of Human Trabecular Bone,” *J. Bone Miner. Res.*, **21**(10), pp. 1608–1617.
- [7] Rice University, 2020, “Bone Structure,” OpenStax.
- [8] Cooper, C., and Melton, L. J., 1992, “Epidemiology of Osteoporosis,” *Trends Endocrinol. Metab.*, **3**(6), pp. 224–229.
- [9] Adams, J. E., 1997, “Single and Dual Energy X-Ray Absorptiometry,” *Eur. Radiol.*, **7**(SUPPL. 2), pp. 20–31.
- [10] GE Healthcare, 2017, “Bone Densitometry Portfolio.”
- [11] Damilakis, J., Adams, J. E., Guglielmi, G., and Link, T. M., 2010, “Radiation Exposure in X-Ray-Based Imaging Techniques Used in Osteoporosis,” *Eur. Radiol.*, **20**(11), pp. 2707–2714.
- [12] U.S. NRC, 2019, “Information for Radiation Workers” [Online]. Available: <https://www.nrc.gov/about-nrc/radiation/health-effects/info.html#dose>.
- [13] Karellas, A., 1992, “Dual-Energy System for Quantitative Radiographic Imaging.”
- [14] Kanis, J. A., 2009, “The Diagnosis of Osteoporosis and the Fracture Risk Assessment,” *Endokrinologiya*, **14**(1), pp. 30–36.
- [15] Pavelko, V., Kuznetsov, S., Nevsky, A., and Marinbah, M., 2017, “Vibration-Based Structural Health Monitoring of the Aircraft Large Component,” *IOP Conf. Ser. Mater. Sci. Eng.*, **251**(1).
- [16] Zhao, L., Huang, X., Zhang, Y., Tian, Y., and Zhao, Y., 2019, “A Vibration-Based Structural Health Monitoring System for Transmission Line Towers,” *Electron.*, **8**(5).
- [17] Shepard, G. D., and Lepanto, J. A., 1992, “Localization of Structural Flaws Using Cross Transfer Function Zeros,” *IFAC Proc. Vol.*, **25**(22), pp. 445–450.
- [18] Phaneuf, A., 2020, “Latest Trends in Medical Monitoring Devices and Wearable Health Technology,” *Bus. Insid.* [Online]. Available: <https://www.businessinsider.com/wearable-technology-healthcare-medical-devices?r=US&IR=T>.
- [19] Turner, C. H., 2002, “Determinants of Skeletal Fragility and Bone Quality,” *J. Musculoskelet. Neuronal Interact.*, **2**(6), pp. 527–528.

- [20] Nugent, M. A., and Esmonde, H., 2015, “Android Application to Assess Smartphone Accelerometers and Bluetooth for Real-Time Control,” *Int. J. Adv. Comput. Sci. Appl.*, **6**(3), pp. 11–19.
- [21] Moticon, 2020, “Moticon Rego AG” [Online]. Available: <https://www.moticon.de/insole3-overview/>.
- [22] Enflux, 2020, “Enflux” [Online]. Available: <https://www.getenflux.com/pages/product>.
- [23] Kim, W., Tan, J., Veloso, A., Vleck, V., and Voloshin, A. S., 2011, “The Natural Frequency of the Foot-Surface Cushion during the Stance Phase of Running,” *J. Biomech.*, **44**(4), pp. 774–779.
- [24] Boyer, K. A., and Nigg, B. M., 2004, “Muscle Activity in the Leg Is Tuned in Response to Impact Force Characteristics,” *J. Biomech.*, **37**(10), pp. 1583–1588.
- [25] Boyer, K. A., and Nigg, B. M., 2006, “Muscle Tuning during Running: Implications of an Un-Tuned Landing,” *J. Biomech. Eng.*, **128**(6), pp. 815–822.
- [26] Boyer, K. A., and Nigg, B. M., 2007, “Quantification of the Input Signal for Soft Tissue Vibration during Running,” *J. Biomech.*, **40**(8), pp. 1877–1880.
- [27] Kita, K., Osu, R., Hosoda, C., Honda, M., Hanakawa, T., and Izawa, J., 2019, “Neuroanatomical Basis of Individuality in Muscle Tuning Function: Neural Correlates of Muscle Tuning,” *Front. Behav. Neurosci.*, **13**(March), pp. 1–7.
- [28] Ziegert, J. C., and Lewis, J. L., 1979, “The Effect of Soft Tissue on Measurements of Vibrational Bone Motion by Skin-Mounted Accelerometers,” *J. Biomech. Eng.*, **101**, pp. 218–220.
- [29] Hight, T. K., Piziali, R. L., and Nagel, D. A., 1978, “Natural Frequency Analysis of a Human Tibia,” *J. Biomech.*, **13**, pp. 139–147.
- [30] Thomsen, J. J., 1990, “Modelling Human Tibia Structural Vibrations,” *J. Biomech.*, **23**(3), pp. 215–228.
- [31] Boileau, P. E., and Rakheja, S., 1998, “Whole-Body Vertical Biodynamic Response Characteristics of the Seated Vehicle Driver. Measurement and Model Development,” *Int. J. Ind. Ergon.*, **22**(6), pp. 449–472.
- [32] Gupta, M., and Gupta, T. C., 2017, “Modal Damping Ratio and Optimal Elastic Moduli of Human Body Segments for Anthropometric Vibratory Model of Standing Subjects,” *J. Biomech. Eng.*, **139**(10), pp. 1–13.
- [33] Klute, G. K., and Berge, J. S., 2004, “Modelling the Effect of Prosthetic Feet and Shoes on the Heel-Ground Contact Force in Amputee Gait,” *Proc. Inst. Mech. Eng.*, **218**(3), pp. 173–182.
- [34] Nikooyan, A. A., and Zadpoor, A. A., 2011, “Mass-Spring-Damper Modelling of the Human Body to Study Running and Hopping-an Overview,” *Proc. Inst. Mech. Eng. Part H J. Eng. Med.*, **225**(12), pp. 1121–1135.
- [35] Kim, W., Voloshin, A. S., and Johnson, S. H., 1994, “Modeling of Heel Strike Transients during Running,” *Hum. Mov. Sci.*, **13**(2), pp. 221–244.
- [36] Fritzen, C. P., 2005, “Vibration-Based Structural Health Monitoring - Concepts and Applications,” *Key Eng. Mater.*, **293–294**(January 2005), pp. 3–18.
- [37] Christopoulou, G. E., Stavropoulou, A., Anastassopoulos, G., Panteliou, S. D., Papadaki, E., Karamanos, N. K., and Panagiotopoulos, E., 2006, “Evaluation of Modal Damping Factor as a Diagnostic Tool for Osteoporosis and Its Relation with Serum Osteocalcin and Collagen I N-Telopeptide for Monitoring the Efficacy of Alendronate in Ovariectomized

- Rats,” *J. Pharm. Biomed. Anal.*, **41**(3), pp. 891–897.
- [38] Bhattacharya, A., Watts, N. B., Davis, K., Kotowski, S., Shukla, R., Dwivedi, A. K., and Coleman, R., 2010, “Dynamic Bone Quality: A Noninvasive Measure of Bone’s Biomechanical Property in Osteoporosis,” *J. Clin. Densitom.*, **13**(2), pp. 228–236.
- [39] Nelson, M. L., Cox, C., Altman, L., Khoury, J., Bhattacharya, A., and Wasserman, H., 2019, “Bone Shock Absorption in Pediatric Patients With Osteogenesis Imperfecta – A Pilot Study to Assess the Potential of This Technique to Detect Differences in Bone Fragility,” *J. Clin. Densitom.*, pp. 1–5.
- [40] Panteliou, S. D., Xirafaki, A. L., Panagiotopoulos, E., Varakis, J. N., Vagenas, N. V., and Kontoyannis, C. G., 2004, “Modal Damping for Monitoring Bone Integrity and Osteoporosis,” *J. Biomech. Eng.*, **126**(1), pp. 1–5.
- [41] Trama, R., Hautier, C., and Blache, Y., 2020, “Input and Soft-Tissue Vibration Characteristics during Sport-Specific Tasks,” *Med. Sci. Sport. Exerc.*, **52**(1), pp. 112–119.
- [42] Mathworks, 2020, *Signal Processing Toolbox: User’s Guide*, The Mathworks Inc., Natick.
- [43] Ku, C. J., and Tamura, Y., 2009, “Rational Fraction Polynomial Method and Random Decrement Technique for Force-Excited Acceleration Responses,” *J. Struct. Eng.*, **135**(9), pp. 1134–1138.
- [44] Schubert, E., Sander, J., Ester, M., Kriegel, H. P., and Xu, X., 2017, “DBSCAN Revisited, Revisited: Why and How You Should (Still) Use DBSCAN,” *ACM Trans. Database Syst.*, **42**(3).
- [45] Mathworks, 2020, “DBSCAN,” *Statistics and Machine Learning Toolbox: User’s Guide*, The Mathworks Inc., pp. 16.19-16.25.
- [46] Kaplan, D., 2012, “Knee Point.”
- [47] Montgomery, D. C., Runger, G. C., and Hubel, N. F., 2010, “Decision Making for Two Samples,” *Engineering Statistics*, Wiley, pp. 230–248.
- [48] Porac, C., and Coren, S., 1977, *Lateral Preferences and Human Behavior*, Springer-Verlag, Berlin.
- [49] Algorithms, R., and Rcpp, L., 2019, “Package ‘DbSCAN.’”
- [50] Frankline, G. F., Powell, J. D., and Workman, M. L., 1997, “System Identification,” *Digital Control of Dynamic Systems*, Addison Wesley Longman, Menlo Park, pp. 479–481.
- [51] Ljung, L., 1999, *System Identification Theory for the User*, Prentice Hall, Upper Saddle River.
- [52] Ljung, L., 2015, “System Identification Toolbox: User’s Guide.”
- [53] Madsen, K., Nielsen, H. B., and Tingleff, O., 2004, “METHODS FOR NON-LINEAR LEAST SQUARES PROBLEMS.”
- [54] Tözeren, A., 2000, “Geometric Properties of the Human Body,” *Human Body Dynamics: Classical Mechanics and Movement*, Springer, New York.